الجمهورية الجزائرية الديمقراطية الشعبية
PEOPLE'S DEMOCRATIC REPUBLIC OF ALGERIA
وزارة التعليم العالي والبحث العلمي
MINISTRY OF HIGHER EDUCATION
AND SCIENTIFIC RESEARCH

جامعة محمد بوضياف ـ المسيلة
MOHAMED BOUDIAF UNIVERSITY - M'SILA
كلية التكنولوجيا
FACULTY OF TECHNOLOGY
قسم الإلكتـــرونيك
ELECTRONICS DEPARTMENT

MASTER THESIS

DOMAIN: SCIENCE AND TECHNOLOGY
SPECIALITY: ELECTRONICS
OPTION: MICROELECTRONICS

THEME

Study of quantum well solar cells based on $CuIn_{1-x}Ga_xSe_2$ absorbers using SCAPS-1D simulator

Proposed and directed by:
Pr. BOUCHAMA Idris

Realized by:
- SALAMANI Maram safàa
- BEDDIAR Abdrrahmen

Order No.:

PROMOTION: 2024/2025

Dedicate

To the one who has always been my support throughout my journey,

*To my **dear mothe**r,*

I dedicate this humble work as a token of love and loyalty,

In appreciation of your sacrifices and your constant prayers for me.

I ask Allah to bless your life and protect you from all harm.

To my brothers and sisters:

Loudjine**, **Sohail**, **Oussama

thank you for your support and love.

To my dear colleagues and friends at work, especially:

Kouidri Fayssal

My gratitude goes to all of you for your support and encouragement.

And to all my friends and classmates, without exception,

You have my deepest thanks and appreciation.

SALAMANI Maram Safàa

Dedicate

To my dear father whose support and patience have always guided me; thank you for being my strength and constant encouragement.

To the soul of my beloved mother whose memory lives on in my heart, I dedicate this work to you and pray that Allah grants you paradise.

I also thank my dear siblings for their unwavering support during challenging times.

To my friends and classmates, your companionship made this journey meaningful. Thank you for every moment we shared.

And to everyone who helped me along the way, even with a word or a prayer, this achievement is yours as much as it is mine.

Beddiar Abderrahmen

Acknowledgement

*First and foremost, we would like to thank Almighty **ALLAH** for strength and patience, and for granting us the health and patience to complete this work.*

I would like to express my appreciation to my supervisor

***Prof. BOUCHAMA Idris,** Thank you for his patience and this valuable advice.*

*I would like to express my deep gratitude to **jury members** who agreed to be part of our discussion comity and I gratefully acknowledge to **Dr. Marc Burgelman** for providing the SCAPS simulation software.*

. I express my sincere thanks to them.

I would like to thank all my friends who help me directly or indirectly in carrying out this work as well as all our teachers from the Electronics Department University of M'sila.

List of Figures

Chapter I: Solar cell structures

Chapter II: Presentation of Scaps-1D simulator

Chapter III: Results and discussions

List of Tables

Table of contents

Chapter III: Results and discussions

General Introduction

General introduction

The global energy crisis-spanning economic, environmental, and social dimensions-calls for an urgent shift toward sustainable and renewable energy sources. Since the 1980s, our ecological footprint has exceeded the Earth's biocapacity clearly highlighting the unsustainability of the current development model [1]. An energy economy based on fossil fuels is no longer viable, due to the depletion of fossil resources, the climate risks caused by excessive greenhouse gas emissions, and the need to ensure secure access to energy [2].

At the same time, global energy demand continues to grow, especially in developing countries, where more than one billion people still lack access to electricity. To meet this rising demand, renewable sources such as hydropower, biomass, wind, and solar energy must be widely adopted. However, due to the intermittent nature and varying storage capabilities of these sources, a complementary and integrated energy strategy is required [3,4].

Among renewable sources, solar energy holds a special place. In just one hour, the sun provides the Earth with as much energy as humanity consumes in an entire year. is particularly promising because it directly converts sunlight into electricity without moving mechanical parts or thermal cycles—and can even function under diffuse light [5].

The first generation of solar cells was based on crystalline silicon, achieving laboratory efficiencies up to 25% for monocrystalline silicon [6]. However, these technologies are expensive due to their complex fabrication processes and high-temperature requirements. This has led to the exploration of alternative materials such as $CuIn_{1-x}Ga_xSe_2$ (CIGS) with $0 \leq x \leq 1$. This direct bandgap semiconductor has a high absorption coefficient and a tenable bandgap based on gallium content, enabling optimization of the solar spectrum absorption. CIGS-based solar cells have achieved laboratory efficiencies exceeding 20%, with promising cost projections [6,7].

Moreover, the integration of quantum well structures in these devices enhances performance by exploiting quantum confinement effects to improve low-energy photon absorption and carrier collection. These devices use multilayer heterostructures where quantum wells are embedded within the CIGS absorber, modifying the electronic density of states and increasing conversion efficiency [8].

This study focuses on the numerical simulation of quantum well solar cells based on CIGS absorbers, using the well-known SCAPS-1D simulation software, which is widely used for

modelling heterojunctions and complex photovoltaic structures. Photovoltaic parameters such as short-circuit current density (J_{sc}), open-circuit voltage (V_{oc}), fill factor (*FF*), and power conversion efficiency are extracted and analysed from current-voltage (J-V) characteristics and quantum efficiency (QE).

The study investigates the impact of various physical and geometrical parameters (e.g., layer thickness, doping levels, and defect densities) on the overall performance of the conventional (substrate) solar cell with and/or without introduction on quantum well system.

This thesis is organized into three main chapters, each addressing a key aspect of the study of CIGS-based solar cells, from fundamental concepts to advanced numerical modeling:

The chapter I provides a comprehensive overview of photovoltaic solar cells, beginning with their historical development and operational principles. It explores the different generations of solar cells, with a particular focus on thin-film technologies. The structure of thin-film solar cells including the window, buffer, and absorber layers, as well as front and back contacts. Special attention is given to various configurations of CIGS ($Cu(In,Ga)Se_2$) solar cells, such as substrate, superstrate, bifacial, and tandem structures.

The chapter II introduces the SCAPS-1D simulation software. It describes the different panels and functions available in the program, including how to define device structures, input material properties, and set boundary conditions. The chapter also covers numerical parameters, spectrum file usage, digital data import, and visualization tools such as energy band diagrams and I–V characteristic panels.

The final chapter presents the numerical simulation results based on CIGS solar cell structures using SCAPS-1D. It begins with an overview of the CIGS material and its advantages, followed by a detailed investigation into the effects of gallium concentration, absorber thickness, acceptor concentration, and defect density on device performance. The chapter further explores the integration of quantum well structures into CIGS solar cells, analyzing how quantum confinement influences efficiency. The effects of well thickness, defect levels, and well depth are evaluated to assess their impact on device behavior.

Each chapter concludes with a summary of key points, and the thesis ends with a general conclusion that synthesizes the major findings and suggests directions for future research.

References

[1] Sachs, J. D., et al. (2019). "Six Transformations to Achieve the Sustainable Development Goals." Nature Sustainability, 2(9), 805–814.

[2] Rockström, J., et al. (2009). "A Safe Operating Space for Humanity." Nature, 461(7263), 472–475.

[3] Pachauri, S., & Spreng, D. (2011). "Energy access for the poor in the developing world." Annual Review of Environment and Resources, 36, 331–351.

{4] Sims, R. E. H., et al. (2008). "Renewable energy: Current and future issues." Renewable and Sustainable Energy Reviews, 12(2), 762–781.

[5] Lewis, N. S., & Nocera, D. G. (2006). "Powering the planet: Chemical challenges in solar energy utilization." Proceedings of the National Academy of Sciences, 103(43), 15729–15735.

[6] Green, M. A., Emery, K., Hishikawa, Y., Warta, W., & Dunlop, E. D. (2010). "Solar cell efficiency tables (version 36)." Progress in Photovoltaics: Research and Applications, 18(5), 346–352.

|7] Saga, T. (2010). "Advances in crystalline silicon solar cell technology for industrial mass production." NPG Asia Materials, 2(3), 96–102.

[8] Martí, A., & Luque, A. (2004). "Next generation photovoltaics: High efficiency through full spectrum utilization." Renewable and Sustainable Energy Reviews, 8(2), 195–208.

Chapter I

Solar cell structures

Chapter I: Solar cell structures

I.1 Introduction

Driven by population growth and increasing prosperity, global energy consumption has experienced rapid growth in recent decades, exceeding 440 EJ in 2021 across various sources such as oil, natural gas, nuclear energy, and renewables [1]. Unfortunately, the escalating use of fossil fuels remains the primary contributor to climate change and poses significant environmental challenges. In 2021, global CO_2 emissions from energy and industrial processes reached 36.1 billion metric tons [2].

Although nuclear energy does not directly emit carbon dioxide, it presents substantial risks to human safety and the environment due to potential accidents and the long-term management of nuclear waste.

To address these concerns and strive for a sustainable future, renewable energies, particularly solar energy, have emerged as a crucial solution. The solar potential on Earth is immense, estimated to be around 10.000 times the current energy consumption of humanity. Solar electricity, including solar photovoltaics is projected to play a significant role, accounting for approximately 20.2% of global electric power by 2026 [3]. Figure I.1 present the cumulative power in function of technology where the photovoltaic energy evaluated quickly between 2010 and 2027.

In this chapter, we provide the fundamental principles of photovoltaic solar cells. We begin by discussing key concepts in the field of solar energy, including solar radiation and air mass. Next, we explain the p-n junction and the photovoltaic effect. We then delve into the functioning and structure of standard photovoltaic cells, exploring their main characteristics and the equivalent circuit model. Additionally, we discuss the various generations of photovoltaic cells. Finally, we present the composition of the cell structure.

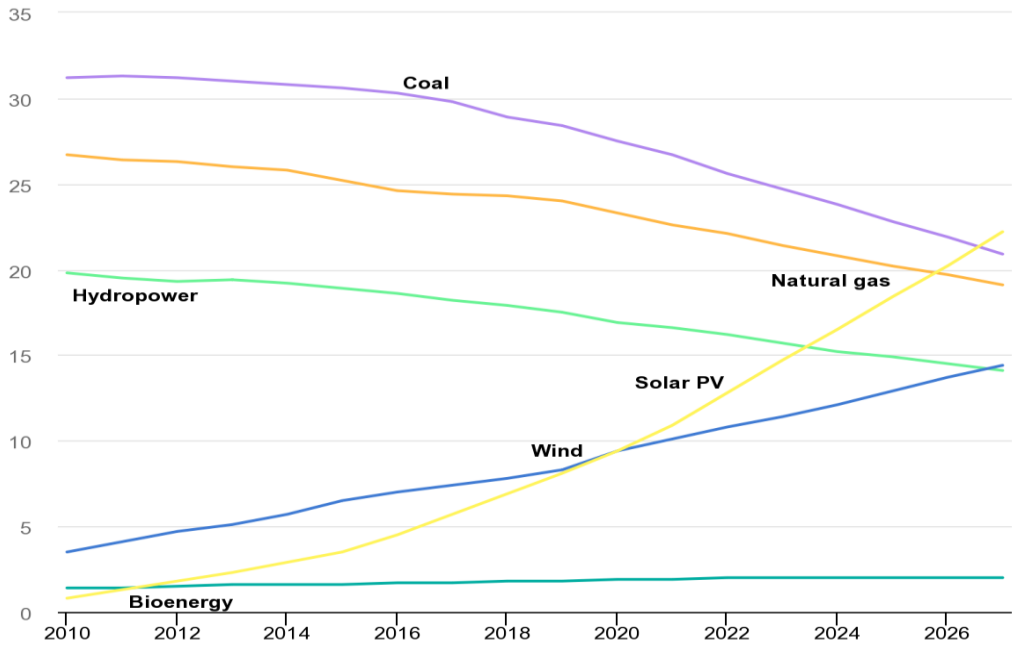

Figure I.1: Cumulative power capacity in function of technology between 2010 - 2027[3].

I.2 History of solar cells

The history of solar cells leading up to 2023 is a tale of innovation, research, and technological advancements. It all began in 1839 when the French physicist Alexandre-Edmond Becquerel discovered the photovoltaic effect, establishing the foundation for solar cell development [4]. However, practical applications did not emerge until much later. In 1954, Bell Laboratories in the United States achieved a significant breakthrough by creating the first silicon solar cell, with a conversion efficiency of around 6% significantly higher than the previous selenium cells [5,6].

During the following decades, researchers and engineers focused on improving efficiency and reducing costs. In the 1970s, spurred by the global energy crisis and nuclear power plants incidents such Three Mile Island (USA 1979) and Tchernobyl (URSS 1986), solar energy gained attention as a viable alternative to fossil fuels. Governments and organizations began investing in research and development, leading to steady progress in solar cell efficiency. By the 1980s, the efficiency had reached around 20%, opening up new possibilities for practical applications.

In the 1990s and early 2000s, advancements in manufacturing techniques and material innovations, such as thin-film solar cells, emerged. These developments allowed for more cost-effective production and expanded the potential applications of solar cells. Additionally, governments worldwide introduced incentives like feed-in tariffs and tax credits to promote solar energy adoption, which further accelerated the growth of the industry.

By the early 21st century, solar cells became increasingly common on rooftops, powering homes and businesses. The push for renewable energy and sustainability led to substantial investments in solar power infrastructure, including the establishment of large-scale solar farms and utility-scale installations.

As the industry progressed, researchers continued to explore new materials and technologies. Emerging technologies like perovskite solar cells and tandem solar cells showed promise in increasing efficiency and reducing costs. Furthermore, the integration of solar cells into building materials and wearable devices became areas of interest, offering new avenues for energy generation.

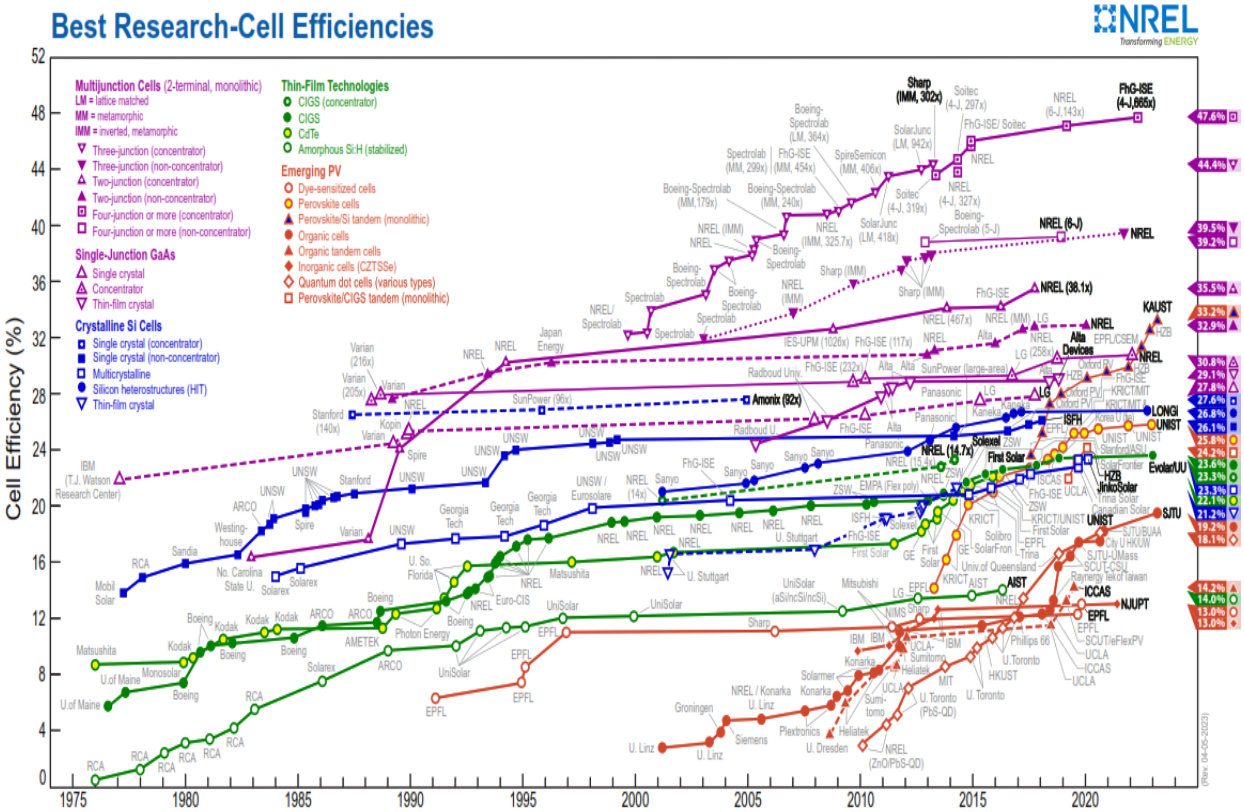

Figure I.2: The highest confirmed conversion efficiencies for research cells for a range of photovoltaic technologies from 1976 [7].

By 2023, solar cells had become a mainstream and rapidly growing segment of the global energy landscape. With increasing efficiency levels, declining costs, and widespread adoption, solar energy played a crucial role in mitigating climate change and transitioning towards a sustainable future. Figure I.2 show the highest confirmed conversion efficiencies for research cells for a range of photovoltaic technologies from 1976, ongoing research and development aimed to further enhance solar cell efficiency, storage capabilities, and integration into smart grids, fueling optimism for a renewable energy revolution powered by the sun.

1.3 Photovoltaic solar cell principal of function

1.3.1 Solar radiation and Air Mass

The Sun emits energy in all directions, and the Earth receives a portion of this energy as it intercepts the solar radiation (Figure I.3). At the top of the Earth's atmosphere, the power flux of solar radiation is measured at 1400 Watts/m^2. However, the Earth's relatively dense atmosphere filters out about 400 Watts/m^2 [8], including a significant portion of ultraviolet rays. These radiations belong to the electromagnetic spectrum, which spans from ultraviolet to infrared wavelengths, with the visible spectrum having the highest intensity.

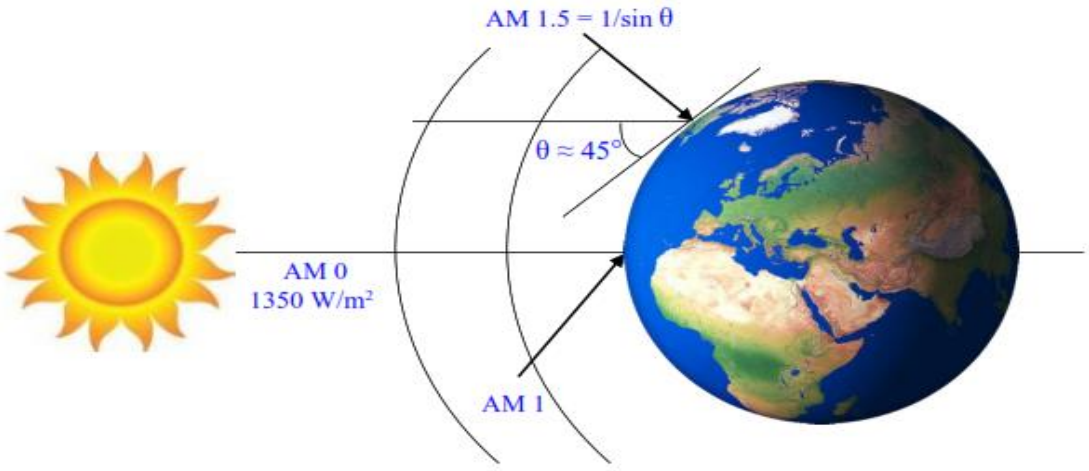

Figure I.3: Air mass in function of sun height angle (θ).

The solar radiation reaching the Earth's surface is influenced by the atmospheric thickness that the light rays traverse, resulting in spatial variations across the globe. To account for the energy loss due to atmospheric absorption, the concept of "Air Mass" is introduced and represented as AMx. The Air Mass value is calculated using the formula AM = 1/sin θ, where θ represents the

solar elevation angle, as illustrated in Figure I.3, 'θ' is the angle between the solar radiation and the horizontal plane on Earth.

Figure I.4 illustrates the spectrum of solar irradiation. Different standards, specifically ASTM G173-03 [9], are employed to describe these spectra: AM0 refers to the solar spectrum observed by satellites outside the atmosphere, characterized by an integrated power density of 1367 W/m^2. Solar cells designed for space applications are optimized for this particular spectrum. AM1.5 represents the spectrum of direct sunlight reaching the Earth's surface when the sun's rays pass through the atmosphere 1.5 times. This corresponds to a zenith angle of 48.19°. The AM1.5 spectrum includes light from a 2.5° cone, totaling 900 W/m^2, and is utilized in concentrating solar power plants. For most applications like flat photovoltaic or thermal modules, the AM1.5G spectrum is employed, totaling 1000 W/m^2. This spectrum combines the direct light from the AM1.5 spectrums with diffuse light resulting from scattering and multiple reflections. Consequently, it intensifies the blue component of the solar spectrum.

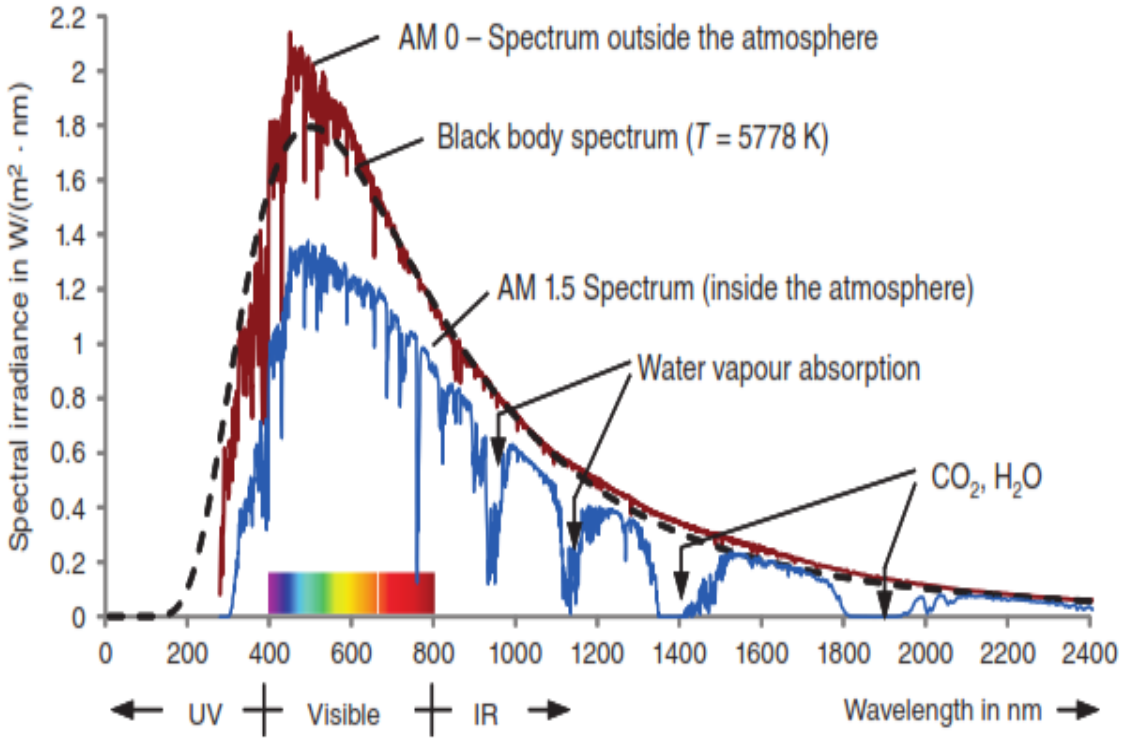

Figure I.4: AM0 and AM1.5 spectrums, outside and inside the atmosphere [8].

1.3.2 Semiconductors

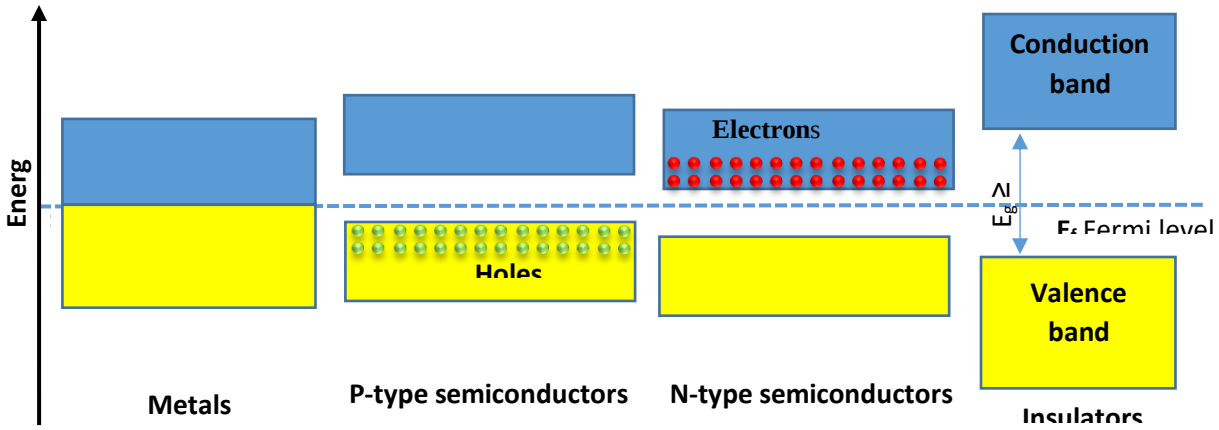

Sigure I.5: Energy diagrams of different type of materials.

Semiconductors are materials that exhibit electrical properties lying between those of conductors and good insulators. When a semiconductor is undoped or in its pure form, it is referred to as an intrinsic semiconductor. In this state, semiconductors do not possess characteristics of either a good insulator or a good conductor. In terms of energy bands, semiconductors have an almost filled valence band and an empty conduction band, with a very small forbidden energy gap, as illustrated in Figure I.5. At a temperature of absolute zero, the conduction band is devoid of electrons, while the valence band is filled. As the temperature increases, the width of the forbidden energy gap decreases. Consequently, some valence electrons gain sufficient energy to transition into the conduction band. This phenomenon leads to an increase in the conductivity of the semiconductor with temperature [10].

Semiconductors can be composed of a single element, such as Ge and Si, or they can be compounds like ZnO, ZnS, InP, GaAs, CdTe, as well as alloys like CIGS or $CZTS_xSe_{1-x}$.

Intrinsic semiconductors have high resistance and allow only a very small amount of current to flow. However, there conducting ability can be significantly modified by introducing specific impurities. When impurities are intentionally added to intrinsic semiconductors, they are referred to as extrinsic semiconductor materials. Extrinsic semiconductors exhibit higher electrical conductivity compared to intrinsic semiconductors, making them suitable for production of electronic devices like diodes and transistors. Several substances can serve as sources of

impurities, including phosphorus (P), arsenic (As), indium (In), boron (B), aluminum (Al), and gallium (Ga). Based on the nature of the added impurities (pentavalent or trivalent), two distinct types of extrinsic semiconductors can be generated.

P-type semiconductor

A p-type semiconductor is created by doping an intrinsic semiconductor with trivalent material (In, B, Al, and Ga). In this type of semiconductor, the majority of charge carriers are holes, resulting in a higher hole density compared to electron density. The acceptor energy level of the p-type semiconductor is situated near the valence band and away from the conduction band.

N-type semiconductor

An n-type semiconductor is formed by doping an intrinsic semiconductor with pentavalent materials (Sb, P, and As) as impurities. In this case, the majority of charge carriers are electrons, while holes are considered minority carriers. The electron density in an n-type semiconductor is significantly higher than the hole density. The donor energy level is positioned near the conduction band and away from the valence band.

I.3.3 P-N junction

To comprehend photovoltaic devices, it is essential to have a fundamental grasp of the p-n junction. A p-n junction semiconductor diode is created by introducing doping of P-type and N-type impurities onto a wafer, as depicted in Figure I.6. The region where the two semiconductor regions meet forms a boundary interface known as the junction. The junction plane theoretically exhibits an equal density of donors and acceptors.

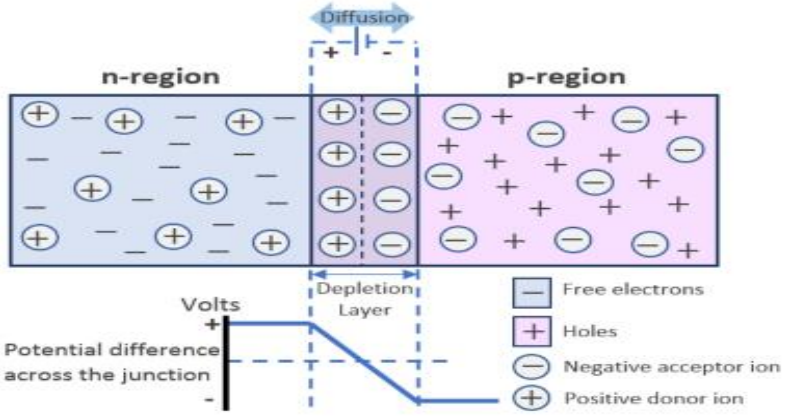

Figure I.6: P-N junction in semiconductors.

P-N junctions are formed in single crystal semiconductors through a process called doping. Several phenomena occur at the junction: When the p-n junction is initially formed, electrons are predominantly located in the N-region, while holes are concentrated in the P-region. Electrons act as minority carriers in the P-region, whereas holes act as minority carriers in the N-region. As the p-n junction is formed, electron diffusion occurs from the N-region to the P-region, resulting in the accumulation of positive charge near the junction. Conversely, hole diffusion takes place from the P-region to the N-region, resulting in the accumulation of negative charge near the junction. This generation of positive and negative charges creates a barrier potential, also known as the depletion layer or VB, as illustrated in Figure 1.6. The depletion layer is rapidly established across the junction and is much thinner compared to the P and N regions.

The barrier potential prevents the flow of charge carriers across the junction, unless provided with external energy from a voltage source. At room temperature (300 K), the barrier potential is approximately 0.7 V for silicon (Si) and 0.3 V for germanium (Ge).

In thermal equilibrium, the potential difference across the junction, referred to as the built-in potential or junction potential, restricts the further movement of charge carriers. The built-in potential is influenced by the doping levels of the P and N regions. when a voltage is applied to the p-n junction externally, it can be forward-biased or reverse-biased:

- **Forward bias**: When the positive terminal of the voltage source is connected to the P-side and the negative terminal to the N-side, the p-n junction is forward-biased. This reduces the potential barrier and allows the majority carriers to move across the junction easily, resulting in a current flow. The forward biased p-n junction is commonly used in diodes and transistors.
- **Reverse bias**: When the positive terminal of the voltage source is connected to the N-side and the negative terminal to the P-side, the p-n junction is reverse-biased. This increases the potential barrier, preventing the majority carriers from crossing the junction. In this state, only a small reverse current (leakage current) flows, primarily due to the minority carriers. The reverse biased p-n junction is often used in diodes as a means of blocking current in one direction.

Usually, one can find five different types of semiconductor junctions that have application in photovoltaic solar cells, Homojunction, Heterojunction, metal-semiconductor junctions, and semiconductor-electrolyte junctions [11].

I.3.4 Photovoltaic effect

Light is made up of packets of energy, called photons, whose energy depends only upon the frequency of the light; the energy of a photon could be calculated using Planck's equation:

$$E = h\nu = c / \lambda \quad (1)$$

Where ν is the frequency of the light in Hz and c is the speed of light in a vacuum ($c = 3 \times 10^8 m/s$), h is the Planck's constant ($h = 6.626 \times 10^{-34}\ Js$).

When light strikes the surface of a pure metal substance and the energy surpasses a certain threshold, electrons within the material are elevated to higher energy levels. However, these excited electrons quickly return to their ground state. In a photovoltaic device, however, an inherent asymmetry prevents the electrons from relaxing and instead directs them towards an external circuit. This process, known as the photovoltaic effect as illustrated in Figure I.7, involves three fundamental steps:

- Generation of charge carriers due to photon absorption;
- Separation of the photo generated charge carriers;
- Extraction of the photo generated charge carriers.

If the energy of the incident photon is sufficiently high ($h\nu = E_g$, where E_g is the band gap energy), the photon can cause an electron to transition from the valence band to the conduction band of the semiconductor material without energy loss, resulting in the creation of an electron-hole pair. These electrons and holes are separated by an internal electric field at the junction and collected between a grid (front side) and a back contact (rear side), and then discharged into the load. If the photon energy is great than the band gap energy $h\nu > E_g$, a part of the energy is thermalized, while if hν > Eg the photon is not absorbed.

Recombination occurs between electron-hole pairs, where the electron falls back to its initial energy state and releases energy either through radiative recombination (photon emission) or non-radiative recombination (transfer of energy to other holes and electrons). The solar cell is designed in such a way that the electron-hole pairs must reach the membrane before recombination can take

place. This requires the time required for these charge carriers to reach their respective membranes to be shorter than their lifetime, which imposes a limit on the thickness of the absorber.

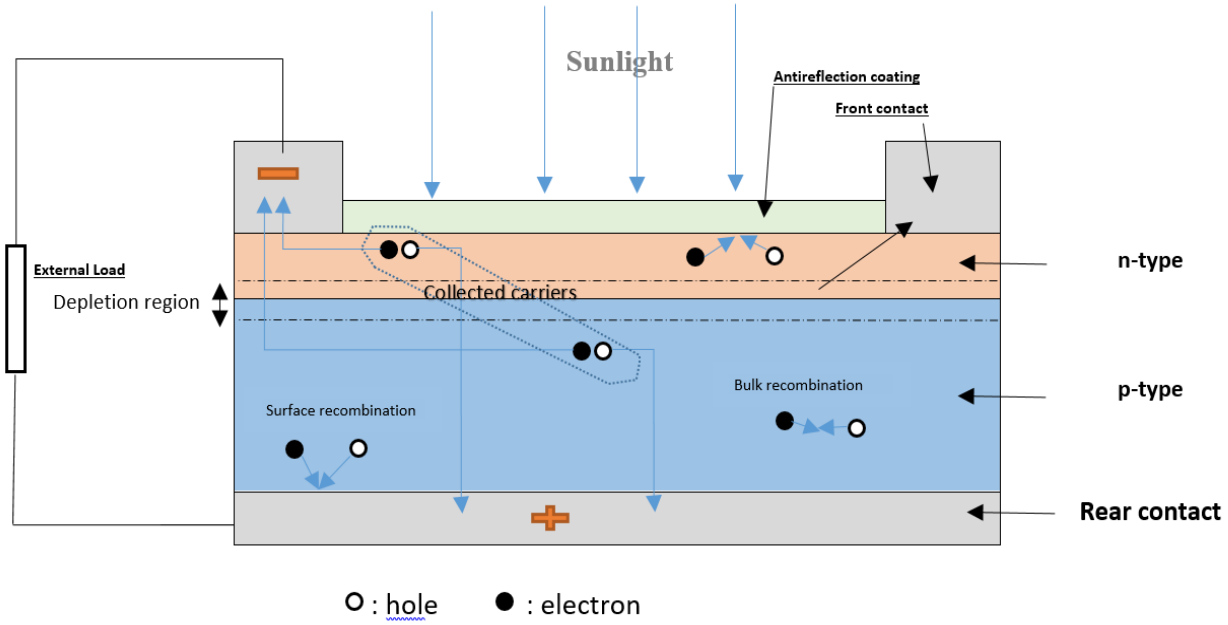

Figure I.7: Generation, separation and collect of charge carrier by photon absorption.

I.4 Different generations of solar cells

Solar cells have undergone substantial advancements over the past forty years, resulting in significant improvements in their power conversion efficiency. Generally, solar cells can be categorized into three types:

I.4.1 First-generation of photovoltaic solar cell: crystalline silicon cells

The initial generation of solar cells is manufactured using silicon wafers. This technology, known as first-generation solar cells, is the oldest and most widely used due to its relatively high-power conversion efficiencies, typically ranging from 15% to 20%. Compared to non-silicon-based solar cells, this technology offers better efficiency and longer lifespan. However, it is more susceptible to efficiency loss at higher temperatures.

W. Shockley and H. Queissier were established that the maximum theoretical power conversion efficiency (PCE) of a single junction solar cell is approximately 33% [12]. Most solar

cells utilizing polycrystalline silicon achieve PCEs around 15% to 20% [13,14]. Mono-crystalline silicon solar cells, on the other hand, have fewer defects in the silicon lattice and typically exhibit higher PCEs, with the highest recorded efficiency reaching 25% [15], but their production and manufacturing costs are relatively expensive. Within the silicon wafer-based technology, there are two subcategories [16-19]:

- Single/Mono-crystalline silicon solar cells;
- Poly/Multi-crystalline silicon solar cells.

I.4.2 Second-generation of solar cells: thin-films solar cell

This cell generation class is also known as thin film solar cells because of using only few micrometer thicknesses of different layer materials in comparison of crystalline silicon based cells. In the past decade, there has been an immense amount of research conducted on the production of more cost effective thin-film solar cells [20].

In this generation, use of silicon wafers is avoided while low-cost material like amorphous silicon, Cadmium Telluride Cds/CdTe, and Cu(In,Ga)Se_2 are used. They are produced by methods such as sputtering, plasma-enhanced chemical vapor deposition and physical vapor deposition. The highest record of PCE for thin-film technology solar cells are 21.1% – 23.3%, certified by National Renewable Energy Laboratory USA. Although their efficiencies due to less crystallized structure and presence of impurities remain lower than those of the first-generation, this type of cells prompted the development of light weight and flexible panels at relatively lower cost.

I.4.3 Third-generation of solar cell

Third-generation solar cells refer to a class of emerging photovoltaic technologies that aim to overcome the limitations of traditional first- and second-generation solar cells. These third-generation cells utilize alternative materials and novel device architectures to achieve higher efficiency, lower cost, and improved functionality. Third-generation solar cell technologies include organic photovoltaic cells with a power-conversion efficiency (PCE) record of 19.31% [21]. Dye-sensitized solar cells (DSSCs) with PCE reaches up to 12% [22]. Quantum dot solar cells: quantum dot solar cells employ nanoscale semiconductor crystals called quantum dots as the light-absorbing layer, but the most promising are:

- Perovskite solar cells: Perovskite solar cells utilize typically hybrid organic-inorganic lead halide compounds, as a light-absorbing layer. They have gained significant attention for their rapid efficiency improvement achieving recently 25.3% efficiency [23].
- Tandem and Multi-junction cells: tandem and multi-junction solar cells combine multiple layers with different bandgaps to capture a wider range of the solar spectrum. By utilizing complementary absorber materials, these cells can achieve higher efficiency levels. Recently scientists led by Saudi Arabia's KAUST have achieved a power conversion efficiency of 33.7% for a perovskite-silicon tandem solar cell [24].

I.5 Thin-film solar cell structure

The key component of a solar cell is the P-N junction, which is formed by connecting a p-type semiconductor (absorber) with an n-type semiconductor (buffer) using various techniques. To optimize the functioning and achieve high efficiency, additional layers may be incorporated. These layers can include a Transparent Conductive Oxide (TCO) layer, as well as an anti-reflective coating (ARC). Figure I.8 illustrates a typical solar cell structure, showcasing these essential elements. We can note the presence of several thin layers within the structure, which typically play a significant role in determining its overall performance. Below, we present the characteristics and functions of each layer:

I.5.1 Window layer

A Transparent Conducting Oxide (TCO), referred as a window layer, is a thin film material known for two significant attributes: Transparency ($\geq 80\%$) and electrical conductivity (103 s.cm-1) [25]. Placed on top of the structure within a solar cell, the TCO layer serves as the front contact. Its main purpose is to enable the passage of visible sunlight, minimizing absorption or reflection, and allowing it to reach the underlying semiconductor layers. Additionally, it provides a conductive pathway for the generated electric current to exit the cell.

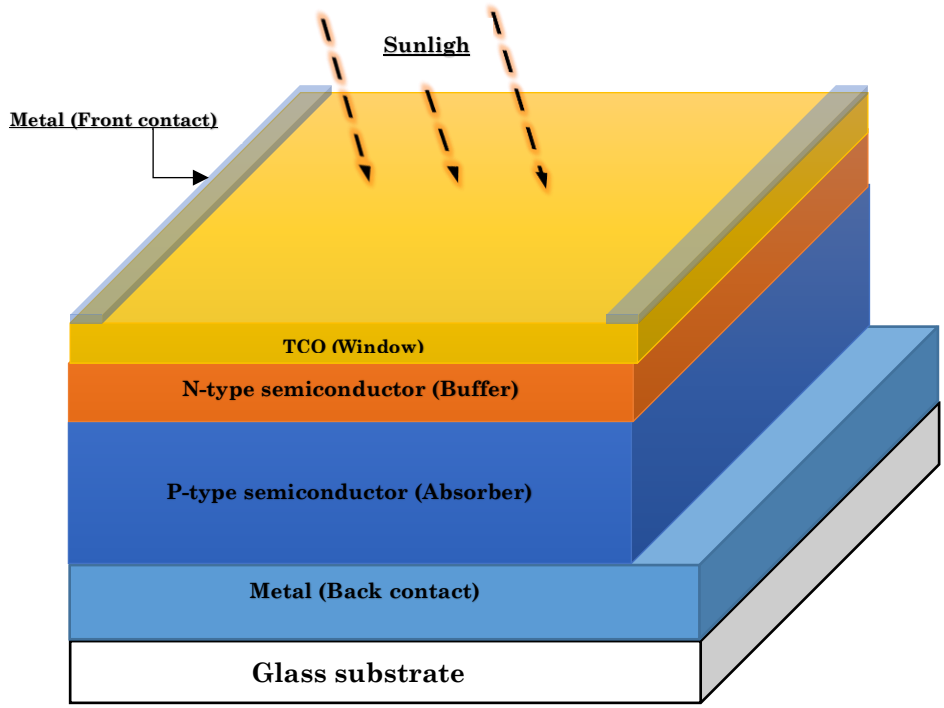

Figure I.8: Schematic representation of a typical solar cell structure.

By incorporating a TCO layer, such as indium tin oxide (ITO), fluorine-doped tin oxide (FTO), ZnO:Al [26], or graphene [27], onto the solar cells, several benefits can be achieved:

- Conductive front contact: The TCO layer provides a conductive pathway for the generated electric current, allowing it to be extracted and utilized in external circuits.
- Electrical isolation: The TCO layer acts as a barrier, electrically isolating the front contact from the underlying semiconductor layers to prevent electrical shorts.
- Anti-reflective properties: In addition to its conductivity, the TCO layer can be engineered with anti-reflective properties to further minimize light reflection and maximize light absorption.

I.5.2 Buffer layer

The buffer layer, positioned between the absorber (p-type semiconductor) and the transparent conducting oxide (TCO), serves the purpose of establishing the P-N junction. In the buffer layer, a wider band-gap layer is typically employed to facilitate maximum light

transmission, minimize absorption losses, and reduce recombination losses. Moreover, it facilitates the efficient transfer of photo-generated carriers to the external circuit and maintains an optimal thickness to minimize series resistance. By optimizing the parameters of the buffer layer, significant improvements can be achieved in the open-circuit voltage (V_{oc}) of solar cells [28]. The buffer layer performs several crucial functions, including:

- Interface optimization: The buffer layer helps to optimize the interface between the absorber and the TCO layer. It acts as a transition layer, ensuring better compatibility between the different materials and minimizing interface defects or energy barriers that could impede the flow of charge carriers.
- Band alignment: The buffer layer can also help align the energy bands between the absorber and the TCO layer. It assists in achieving a favorable band alignment, which promotes efficient charge carrier collection and reduces losses due to carrier recombination at the interfaces.
- Carrier transport: The buffer layer facilitates the transport of charge carriers, both electrons and holes, from the absorber to the TCO layer. It provides a pathway for the charge carriers to move through and reach the front contact, improving the overall conductivity and current collection efficiency of the solar cell.
- Surface passivation: In certain cases, the buffer layer may serve as a surface passivation layer. It helps to reduce surface recombination by minimizing defects or trap states at the absorber surface.

The selection of materials for the buffer layer relies on the specific requirements of the solar cell structure and the type of absorber material employed. Typically, cadmium sulfide (CdS) [29,30] is a commonly used buffer layer material. However, CdS possesses a relatively narrow bandgap (E_g = 2.4 eV), which typically results in parasitic absorption of the incoming light that does not contribute to the photocurrent. CdS is not a perfect buffer layer material, also Cadmium and its compounds are known to be carcinogenic. Initially, Cadmium-free options such as ZnS and $In(OH)_3$ [31] were investigated. Another approach involves utilizing a $ZnO_{1-x}S_x$ buffer layer in conjunction with an ALD-grown $Zn_{1-x}Mg_xO$ as the second buffer layer [32]. Furthermore, Molybdenum disulfide (MoS_2) [33] has also been considered as a potential buffer layer material.

I.5.3 Absorber layer

The absorber layer holds great importance within the solar cell as it serves a critical function of capturing photons from sunlight and converting them into electron-hole pairs. It is typically constructed using a p-type semiconductor material that possesses a band-gap energy aligned with the photon-rich region of the solar spectrum. Common materials used include silicon (Si), amorphous silicon (a-Si), gallium arsenide (GaAs), cadmium telluride (CdTe), indium phosphide (InP), copper indium gallium selenide ($Cu(In,Ga)Se_2$) and copper zinc tin sulfide (CZTS) [34].

The thickness of the absorber layer is carefully selected to optimize the absorption of light while minimizing losses caused by recombination. Typically, it is selected within the range of the charge carrier diffusion length (DL) to facilitate effective collection and extraction of the generated current.

Among the mentioned materials, CIGS and/or CIGSe absorber layers offer several advantages:

- They provide a more sustainable and environmentally friendly alternative compared to CZTS, CZTSe and CdTe.
- $Cu(In,Ga)S_2$ and $Cu(In,Ga)Se_2$ have direct energy bandgaps ranging from 1.5 eV to 2.43 eV and from 1.04 eV to 1.68 eV, respectively, making them well-suited for efficient absorption of solar radiation.
- These materials exhibit high optical absorption coefficients above 10^5 cm^{-1}, indicating their ability to effectively capture photons and convert them into electrical energy [35].
- The charge carrier diffusion lengths for CIGSSe is in the range of 2 -3.6 µm [36]. This allows for a thinner absorber layer, typically around 1 - 4 µm, reducing material usage while maintaining high performance.

The choice of absorber material depends on various factors: including cost, efficiency, stability, and compatibility with other layers in the solar cell structure.

1.5.4 Front and Back contacts

The back contact in the solar cell plays a critical role in collecting and effectively conducting the generated electrical current from the absorber layer to the external circuit. Commonly used materials for the back contact include metals like aluminum (Al), silver (Ag), molybdenum (Mo),

and indium tin oxide (ITO). The choice of the back contact material depends on the specific absorber used in the solar cell.

To establish an efficient charge carrier transport, the back contact must form an ohmic contact with the absorber layer, ensuring a low resistance interface. The work function (W_b) of the back contact material plays a significant role in determining the Schottky barrier height between the rear contact and the absorber layer. Increasing the work function can decrease the Schottky barrier height, enabling better hole carrier collection at the back contact [37].

However, molybdenum (Mo), which is commonly used as a back contact material in CIGS and CdTe thin film solar cells, is not suitable for CZTS absorbers. This is because:

- CZTS has a bandgap of 1.54 eV and an electron affinity of 4.5 eV. Mo has a low work function value, leading to the formation of a Schottky barrier on the p-type CZTS/Mo interface [38].
- During thermal processing, the CZTS absorber layer may decompose into Cu_2S, ZnS, and SnS, while MoS_2 can grow, further hindering its suitability.

I.6 Solar cell configuration using CIGS absorber layer

Cu (In,Ga)Se_2 absorber-based solar cells are thin-film solar cells that utilize CIGS as the semiconductor material in the absorber layer. These solar cells have gained attention as a promising alternative to traditional photovoltaic technologies due to:

- The constituent elements of CIGS are abundant in the earth's crust, making CIGS a sustainable and environmentally friendly choice.
- CIGSe has a band-gap range of 1.04 to 1.68 eV, which aligns well with the solar spectrum, allowing for efficient absorption and conversion of sunlight into electricity.
- CIGSe solar cells are typically fabricated as thin films using deposition techniques like sputtering, chemical vapor deposition (CVD) and/or electrodeposition techniques. The thin-film structure enables lightweight and flexible solar cell designs, making them suitable for curved surfaces and portable devices.

I.6.1 Substrate configuration of CIGSe thin-film solar cell

Similar to CIGS thin-film solar cells (CIGS TFSC), a conventional CIGSe TFSC follows the substrate structure configuration. In this structure, the solar cell device as indicated in Figure I.9(a), it consists of:

- Back contact metal (Mo, Ni and ITO) coated glass substrate with thickness of 800 nm.
- CIGSe layer with a thickness ranging from 1 µm to 5 µm, acts as the light absorber in the solar cell.
- Buffer layer of 0.1 µm to 0.2 µm n-type semiconductor material (CdS, ZnS and ZnO) placed on top of the CIGSe absorber layer to form a P-N junction.
- A thin layer of transparent conductive oxide (TCO), often ZnO:Al, deposited on top of the buffer layer.
- Electrical contact: An electrical contact layer typically made of aluminum (Al) and nickel (Ni).

I.8.2 Superstrate configuration of CIGSe thin-film solar cell

As mentioned in previous paragraph, CIGSe and Mo interface is chemically unstable during thermal processing. To overcome these drawbacks, superstrate configuration is proposed as a solution to this problem. As shown in Figure I.15(b) the back contact in this architecture consists of transparent conductive oxide electrode (FTO or ITO). This electrode serves as the foundation for depositing all other layers involved in electron transport, such as photoactive CIGSe layer. Simultaneously, the transparent nature of the transparent conductive oxide and the glass enables the passage of light.

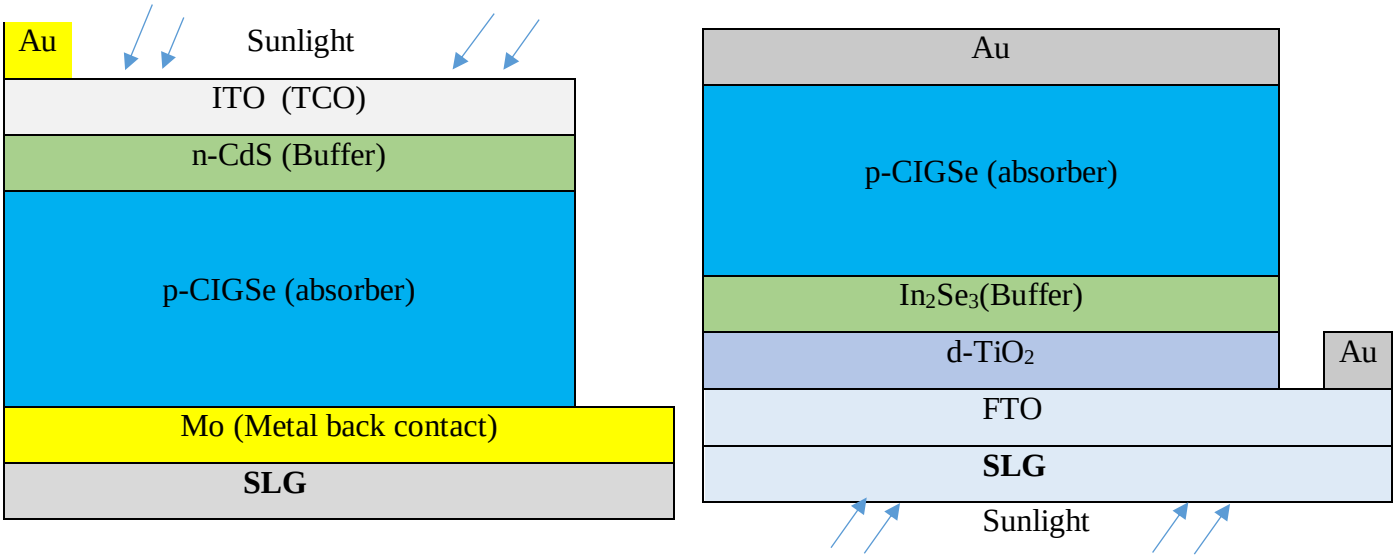

Figure I.9: (a) Substrate configuration and (b) Superstrate configuration of CIGSe solar cell.

I.6.3 Bifacial configuration of CIGSe solar cell

Bifacial configuration of CIGSe solar cell, as shown in Figure I.10, are designs that enable the sunlight to pass from both sides of the cell. This configuration takes advantage of the albedo effect, which refers to the reflection of sunlight by surrounding surfaces in the solar installation area. Bifacial flexible CIGSe solar cell as proposed by Hui Deng [39], this structure achieve an efficiency of 9.3% for the front side and 9% for the backside [39].

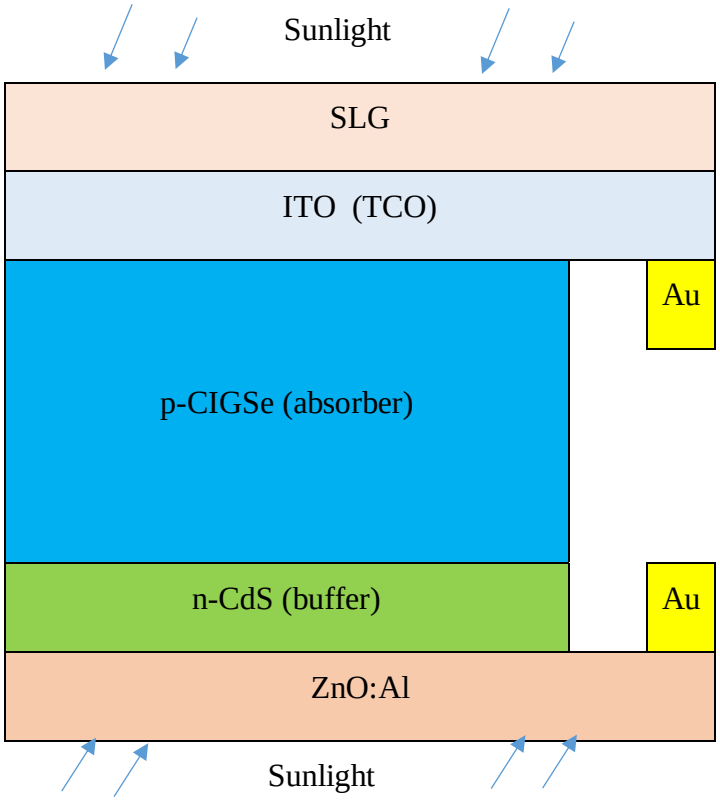

Figure I.10: Bifacial configuration of CIGSe solar cell.

I.6.4 Tandem CIGSe solar cell

The aim of tandem CIGSe thin-film solar cells also known as multi-junction solar cells is to enhance the efficiency of CIGSe-based photovoltaic devices by combining multiple absorber layers with different band-gaps. Various multi-junctions cell configurations have been proposed. Figure I.11 represent a CZTS/Si tandem devices as demonstrated experimentally by A.Haji jafarassar et *al.* [39]. The CZTS layer is designed to absorb higher-energy photons, while the Si layer absorbs lower-energy photons, maximizing the utilization of the solar spectrum.

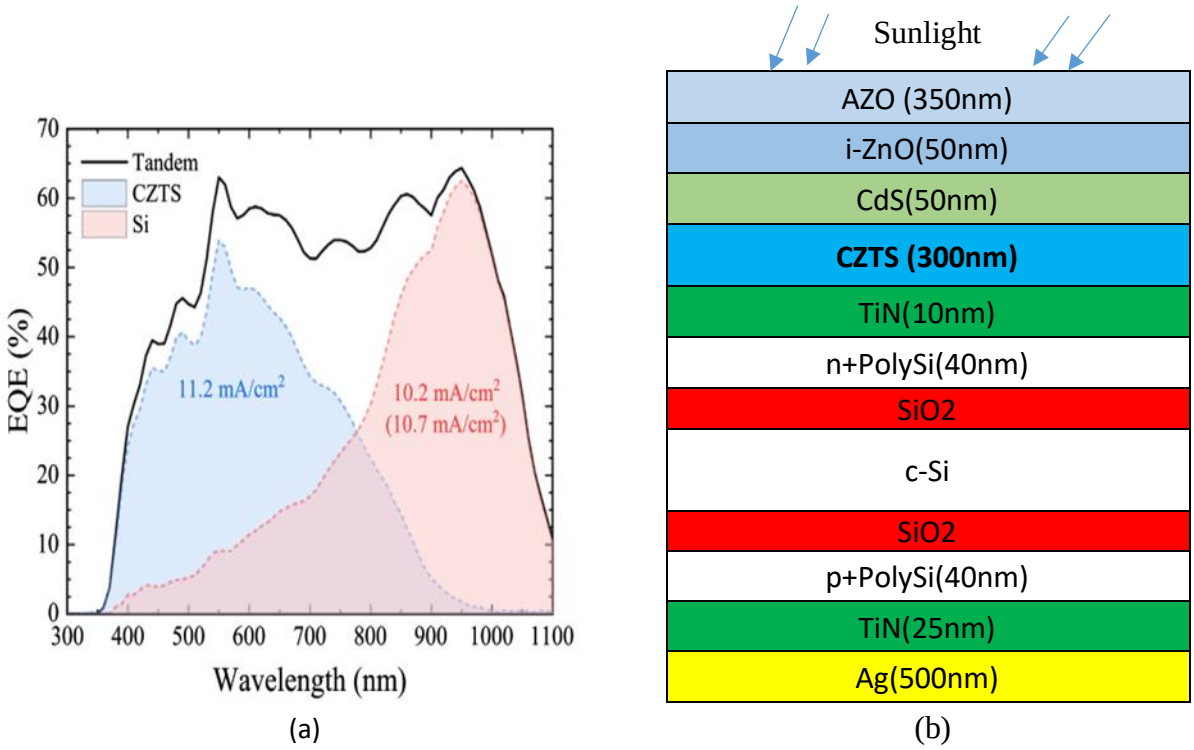

Figure I.11: (a) EQE of both CZTS and c-Si sub-cells and that of Tandem CZTS/c-Si contribution and (b) A.Haji jafarassar et *al.* Tandem solar cell scheme [39].

I.7 Conclusion

This chapter provided an overview of the principal functioning of photovoltaic solar cells, starting from sunlight and progressing to the modeling of thin films solar cell. The P-N junction, was discussed in detail, followed by working mechanisms explanation. The chapter concluded with a focus on the structure of CIGSe solar cells and the various configuration options available.

In the following chapter, we will discuss the SCAPS-1D tool constitution, which is commonly used in thin-film solar cells modelling. A simulation study using SCAPS-1D software was presented for multiple configurations.

References

[1] International Energy Agency, I. (2022). Energy Efficiency 2022. www.iea.org.

[2] Taseska, T., Yu, W., Wilsey, M. K., Cox, C. P., Meng, Z., Ngarnim, S. S., & Müller, A. M. (2023). Analysis of the Scale of Global Human Needs and Opportunities for Sustainable Catalytic Technologies. Topics in Catalysis. https://doi.org/10.1007/s11244-023-01799-3

[3] International Energy Agency, I. (2022). Renewables 2022. www.iea.org.

[4] Fatet, J. (2005). Les recherches d'Edmond Becquerel sur la nature de la lumière entre 1839 et 1843 Histoire d'une interaction réussie entre science et photographie. Claude Bernard university Lyon 1, France.

[5] Chapin, D. M., Fuller, C. S., & Pearson, G. L. (1954). A new silicon p-n junction photocell for converting solar radiation into electrical power. Journal of Applied Physics, Vol. 25, Issue 5, pp. 676–677. https://doi.org/10.1063/1.1721711.

[6] Lincot, D. (2017). The new paradigm of photovoltaics: From powering satellites to powering humanity. Comptes Rendus Physique, Vol. 18, Issues 7–8, pp. 381–390. https://doi.org/10.1016/j.crhy.2017.09.003.

[7] https://www.nrel.gov/pv/cell-efficiency.html, National Renewable Energy Laboratory (NREL), Consulted on June 18, 2023.

[8] Mertens, K., Photovoltaics: Fundamentals, Technology and Practice, John Wiley & Sons, Chichester, UK, 2014, p. 24.

[9] Wenham, S. R. (2007). Applied photovoltaics. Earthscan.

[10] UMESH, K. M., & JASPRIT, S. (2008). Semiconductor device physics and design, Netherlands, Springer, ISBN 978-1-4020-6481-4.

[11] Messei,N. (2016). Study of the effect of grading in composition on the performance of thin film solar cells based on AlGaAs and CZTSSe, a numerical simulation approach. Doctorate thesis, university frères Mentouri Constantine1, Algeria.

[12] Shockley, W., & Queisser, H. J. (1961). Detailed balance limit of efficiency of p-n junction solar cells. Journal of Applied Physics, Vol. 32(3), pp. 510–519. https://doi.org/10.1063/1.1736034.

[13] Jay, F., Muñoz, D., Desrues, T., Pihan, E., Amaral De Oliveira, V., Enjalbert, N., & Jouini, A. (2014). Advanced process for n-type mono-like silicon a-Si:H/c-Si heterojunction solar cells with 21.5% efficiency. Solar Energy Materials and Solar Cells, Vol. 130, pp. 690–695. https://doi.org/10.1016/j.solmat.2014.02.02.

[14] Park, K. M., Lee, M. B., & Choi, S. Y. (2015). Investigation of surface features for 17.2% efficiency multi-crystalline silicon solar cells. Solar Energy Materials and Solar Cells, Vol. 132, pp. 356–362. https://doi.org/10.1016/j.solmat.2014.07.023.

[15] Green, M. A., Emery, K., Hishikawa, Y., Warta, W., & Dunlop, E. D. (2013). Solar cell efficiency tables (version 41). Progress in Photovoltaics: Research and Applications, Vol. 21(1), pp. 1–11. https://doi.org/10.1002/pip.2352.

[16] Chopra, K. L., Paulson, P. D., & Dutta, V. (2004). Thin-film solar cells: An overview. Progress in Photovoltaics: Research and Applications, *Vol.* 12(2–3), pp. 69–92. https://doi.org/10.1002/pip.541.

[17] Fahrenbruch, A.L. and Bube, R.H. (1983). Fundamentals of Solar Cells. Academic Press Inc., New York.

[18] Mohammad Bagher, A. (2015). Types of solar cells and application. American Journal of Optics and Photonics, Vol. 3(5), pp. 94. https://doi.org/10.11648/j.ajop.20150305.17.

[19] Srinivas, B., Balaji, S., Nagendra Babu, M. and Reddy, Y.S. (2015). Review on Present and Advance Materials for Solar Cells. International Journal of Engineering Research-Online, Vol. 3, pp. 178-182.

[20] Komilian, S. (2019). Investigation into Device Optimisation of Organic Solar Cells Using Narrow Bandgap Polymer and the Role of Acceptor Material. Journal and Volume and pp.Link?.

[21] Fu, J., Fong, P. W. K., Liu, H., Huang, C. S., Lu, X., Lu, S., Abdelsamie, M., Kodalle, T., Sutter-Fella, C. M., Yang, Y., & Li, G. (2023). 19.31% binary organic solar cell and low non-radiative recombination enabled by non-monotonic intermediate state transition. Nature Communications, Vol. 14(1), pp. 1760. https://doi.org/10.1038/s41467-023-37526-5.

[22] Sharma, K., Sharma, V., & Sharma, S. S. (2018). Dye-Sensitized Solar Cells: Fundamentals and Current Status. Nanoscale Research Letters. Vol. 13. pp. Springer New York LLC. https://doi.org/10.1186/s11671-018-2760-6.

[23] Yang, T., Gao, L., Lu, J., Ma, C., Du, Y., Wang, P., Ding, Z., Wang, S., Xu, P., Liu, D., Li, H., Chang, X., Fang, J., Tian, W., Yang, Y., Liu, S., & Zhao, K. (2023). One-stone-for-two-birds strategy to attain beyond 25% perovskite solar cells. Nature Communications, Vol. 14(1), pp. . https://doi.org/10.1038/s41467-023-36229-1.

[24] https://www.pv-magazine-india.com, Consulted on June 20, 2023.

[25] Stadler, A. (2012). Transparent conducting oxides - An up-to-date overview. Materials, Vol. 5(12), pp. 661–683. https://doi.org/10.3390/ma5040661.

[26] Kawashima, T., Ezure, T., Okada, K., Matsui, H., Goto, K., & Tanabe, N. (2004). FTO/ITO double-layered transparent conductive oxide for dye-sensitized solar cells. Journal of Photochemistry and Photobiology A: Chemistry, Vol. 164(1–3), pp. 199–202. https://doi.org/10.1016/j.jphotochem.2003.12.028.

[27] Patel, K., & Tyagi, P. K. (2015). Multilayer graphene as a transparent conducting electrode in silicon heterojunction solar cells. AIP Advances, Vol. 5(7). pp. https://doi.org/10.1063/1.4927545.

[28] Sozzi, G., Troni, F., & Menozzi, R. (2014). On the combined effects of window/buffer and buffer/absorber conduction-band offsets, buffer thickness and doping on thin-film solar cell performance. Solar Energy Materials and Solar Cells, Vol. 121, pp. 126-136. https://doi.org/10.1016/j.solmat.2013.10.037.

[29] Niki, S., Contreras, M., Repins, I., Powalla, M., Kushiya, K., Ishizuka, S., & Matsubara, K. (2010). CIGS absorbers and processes. Progress in Photovoltaics: Research and Applications, Vol. 18(6), pp. 453-466. https://doi.org/10.1002/pip.969.

[30] Katagiri, H., Jimbo, K., Maw, W. S., Oishi, K., Yamazaki, M., Araki, H., & Takeuchi, A. (2009). Development of CZTS-based thin film solar cells. Thin Solid Films, Vol. 517(7), pp. 2455-2460. https://doi.org/10.1016/j.tsf.2008.11.002.

[31] Hariskos, D., Spiering, S., & Powalla, M. (2005). Buffer layers in Cu(In,Ga)Se_2 solar cells and modules. Thin Solid Films, Vol. 480–481, pp. 99-109. https://doi.org/10.1016/j.tsf.2004.11.118.

[32] Nakamura, M., Yamaguchi, K., Kimoto, Y., Yasaki, Y., Kato, T., & Sugimoto, H. (2019). Cd-Free Cu(In,Ga)$(Se,S)_2$ thin-film solar cell with record efficiency of 23.35%. IEEE Journal of Photovoltaics, Vol. 9(6), pp. 1863-1867. https://doi.org/10.1109/JPHOTOV.2019.2937218.

[33] Musztyfaga-Staszuk, M., Czupryński, A., & Radev, R. (2022). Review of the Chosen Methods of Producing Front Contacts to Transparent Conductive Oxides Layers in Photovoltaic Structures. Energies, Vol. 15(23), pp. MDPI. https://doi.org/10.3390/en15239026.

[34] Miles, R. W. (2006). Photovoltaic solar cells: Choice of materials and production methods. Vacuum, Vol. 80(10), pp. 1090–1097. https://doi.org/10.1016/j.vacuum.2006.01.006.

[35] Web, J., Muhamad, S. A., & Lafta, M. H. (Year). The CZTS Thin-Film Using Tandem and Multi-junction Solar Cell. Advanced in Engineering and Intelligence Systems Strategic Review, Vol. pp. Link?

[36] Gokmen, T., Gunawan, O., & Mitzi, D. B. (2013). Minority carrier diffusion length extraction in $Cu_2ZnSn(Se,S)_4$ solar cells. Journal of Applied Physics, Vol. 114(11), pp. . https://doi.org/10.1063/1.4821841.

[37] Bouchama, I., & Ali-Saoucha, S. (2017). Effect of wide band-gap TCO properties on the bifacial CZTS thin-films solar cells performances. Optik, Vol. 144, pp. 370–377. https://doi.org/10.1016/j.ijleo.2017.07.009.

[38] Scragg, J. J., Wätjen, J. T., Edoff, M., Ericson, T., Kubart, T., & Platzer-Björkman, C. (2012). A detrimental reaction at the molybdenum back contact in $Cu_2ZnSn(S,Se)_4$ thin-film solar cells. Journal of the American Chemical Society, Vol. 134(47), pp. 19330-19333. https://doi.org/10.1021/ja308862n.

[39] Hajijafarassar, A., Martinho, F., Stulen, F., Grini, S., López-Mariño, S., Espíndola-Rodríguez, M., Döbeli, M., Canulescu, S., Stamate, E., Gansukh, M., Engberg, S., Crovetto, A., Vines, L., Schou, J., & Hansen, O. (2020). Monolithic thin-film chalcogenide–silicon tandem solar cells enabled by a diffusion barrier. Solar Energy Materials and Solar Cells, Vol. 207, pp. https://doi.org/10.1016/j.solmat.2019.110334.

Chapter II

Presentation of SCAPS-1D Simulator

Chapter II: Presentation of SCAPS-1D simulator

II.1. Introduction

SCAPS-1D (The One-Dimensional Solar Cell Capacity Simulator) was developed to simulate the electrical characteristics of a thin-film heterojunction solar cell in the dark or under illumination [1,2]. This simulator allows us to see the I(V) characteristic close to the real case. It is intended to broadly simulate CdTe and Cu (In,Ga)Se_2 thin film solar cells [3].

The SCAPS-1D program finds solutions for structures that consist of an arbitrary number of layers of the semiconductor, with arbitrary dopant profiles (as a position function), with arbitrary energy distributions of deep acceptor levels and/or or donors (single as well as uniform level, Gau□ or tail distribution) in the semiconductor charge and at the heterojunction interfaces (surface states), for arbitrary spectra of light (e.g. superposition of monochromatic lights or AM1.5G light). The permitted spectrum (in an arbitrary frequency band) can be calculated for each operating point (applied voltage, illumination and temperature).

II.2. Different panels in SCAPS-1D program

The program consists of several panels (or windows, or pages). The main panel is the action “panel”. It allowed us to pose the problem and list the requested calculation, execute the calculations, enter other panels, save and draw the results and also exit the program.

The EXIT button on the action panel is the only tool to exit the program see (Figure II.1).

Figure II.1 : Exit window

The other panels are the “EB, IV, AC, CV, Cf and QE” panels. They are used to display results of energy band calculations, and of IV, AC, CVS, Cf and QE calculations if these had been carried away. Finally, there are secondary panels which are only used when the user is asked to enter data, select files or confirm choices. Switching between panels is when clicking the corresponding buttons with the mouse.

II.2.1. Creation, modification and use a Definition File

When the program starts the first window is the action panel. The complete problem organization is contained in afile, it is a text format file with extension (.def) and has the name (problem definition file).

By clicking the "calculate new" button in the action panel, you can load an existing definition file or create a new definition file (create new). When there is already a definition file in active memory, it can be modified (edited). When starting, (create new) and (edit) are equivalent. Now we will discuss in detail how to install a problem.

II.2.2. Construction of a New Definition File or the Editing of an Existing

In the following, the word left means the rear contact, the word right is the other side. The light is always incident on the contact in front, i.e. on the right.

After clicking the "Create New" or "Edit" options, the Solar Cell Definition panel is active. It allows the user to create a structure and define all its characteristics. It allows up to 9 layers. The first layer is the back contact, and the last is the front contact. The user can specify the properties of the intermediate semiconductor layers (max. 7). For each layer, up to three different SRH recombination centers (discrete or distributed in energy) can be defined, and also for interface recombination [5].

II.2.3. Rear Contact

If the rear contact button is pressed (see Figure II.2), its properties can be set: a velocity parameter for electron and holes and information on the output work. If the (OK) button is pressed the data is accepted, and the solar cell definition panel reappears. The meaning of the parameters is as follows:

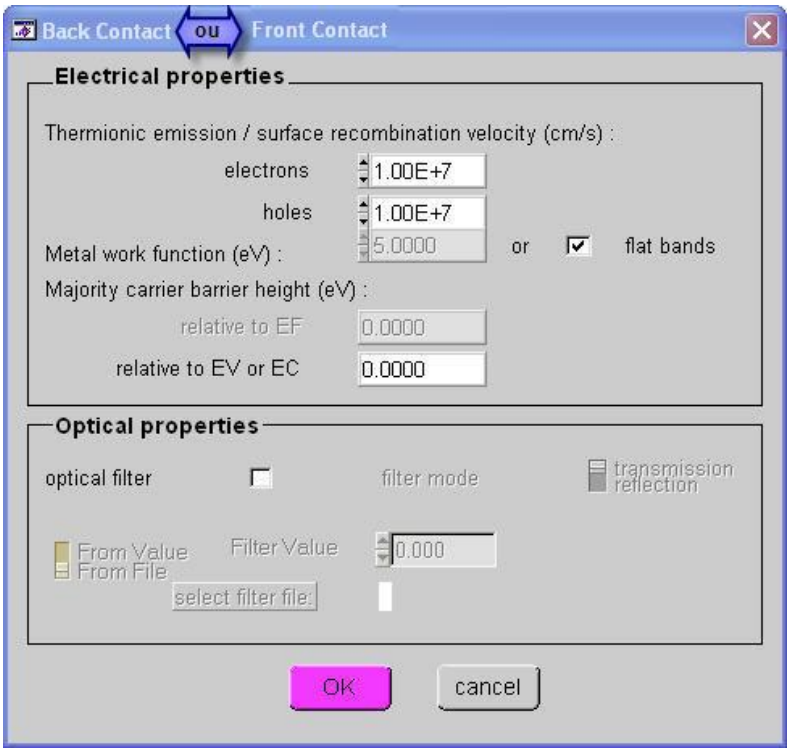

Figure II.2: Rear or front contact window

1) for majority carriers, the model is that of thermionic emission. The meaning of the velocity parameter is thermal velocity v_{th}. The majority carrier current $j_{c,maj}$ at back contact is given by:

$$j_{c,\mathrm{maj}} = \mathrm{q}v_{\mathrm{th}} N_C \exp\left(-\frac{q\Phi_B}{\mathrm{kT}}\right)\left(\exp\left(\frac{\mathrm{q}V_c}{\mathrm{kT}}\right) - 1\right) \qquad \text{(II.1)}$$

$$j_{c,\mathrm{maj}} = \mathrm{q}v_{\mathrm{th}} N_V \exp\left(-\frac{q\Phi_B}{\mathrm{kT}}\right)\left(\exp\left(\frac{\mathrm{q}V_c}{\mathrm{kT}}\right) - 1\right) \qquad \text{(II.2)}$$

Depending on the type of majority carriers (electrons or holes respectively); V_{CIS} the step of the voltage on the contact. The height of the barrier is calculated from the work function Φ_m of the metal, the electron affinity χ and the gap band Eg:

$$\Phi_B = \Phi_m - \chi \qquad \text{(p-type; the electron barrier height).} \qquad \text{(II.3)}$$

$$\Phi_B = \chi + E_g - \Phi_m \text{ (n-type; the barrier height of the holes).} \qquad \text{(II.4)}$$

2) For minority carriers, the model is the classical description of minority carrier surface recombination. The meaning of the velocity parameter is speed of recombination of the

minority carrier then. The minority carrier current $j_{c,min}$ behind contact is therefore given by:

$$j_{c,\min} = qS_c(c - c_0) \quad \text{(II.5)}$$

Where c denotes concentration of the electron or hole, and the*c0*denotes the concentration of the balance of electrons or holes in contact with the back.

3) The metal work function Φ_m (for majority carriers) can be entered by the user. However, the user can also choose the flat "strips" option. In this case, SCAPS calculates for each temperature the metal work function Φ_m in such a path that the flat band conditions predominate:

$$\Phi_m = \chi + \ln\left(\frac{N_C}{N_d - N_a}\right) \text{(n-type)} \quad \text{(II.6)}$$

$$\Phi_m = \chi + E_g - \ln\left(\frac{N_C}{N_a - N_d}\right) \text{(p-type)} \quad \text{(II.7)}$$

Here, *Nd* represents the shallow donor concentration and Na for the shallow acceptor concentration, specified in the layer definition. Although this option does not correspond to a physical situation, it allows the user to define a perfect ohmic contact conveniently.

4) All parameters relevant to back contact are assumed to be independent of temperature.

II.2.4. Semiconductor layers

If the (add layer) button is pressed in the solar cell definition panel (Figure II.3), the layer characteristics can be defined in a new screen. The user can now enter the layer name and properties.

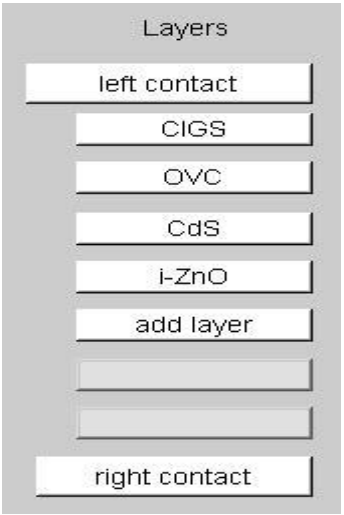

Figure II.3: The Semi-conductor's layers.

When the right mouse button is clicked, with the cursor placed at one of the layers of the semiconductor, a menu appears which allows the user to duplicate and remove an already existing layer. allows the user to duplicate and remove an already existing layer. When the (duplicate) option is chosen, the new layer is inserted below the already existing layer. A new interface is created between the recently created layer and the previous one. When the (remove) option is chosen, the selected layer and the previous interface are removed from the structure.

Remarks

1) The densities of states in the conduction band and the valence band, NC and NV, depend on temperature as:

$$N_C(T) = N_{C0}\left(\frac{T}{T_0}\right)^{1.5} \quad \text{(II.8)}$$

$$N_V(T) = N_{V0}\left(\frac{T}{T_0}\right)^{1.5} \quad \text{(II.9)}$$

Where the reference temperature T0 equals 300 K. The reference evaluates NC0 and NV0 at room temperature are the values to be specified. The thermal velocity vth(T) depends on temperature as:

$$v_{\text{th}}(T) = v_{\text{th}0}\left(\frac{T}{T_0}\right)^{0.5} \quad \text{(II.10)}$$

Again, the value v_{th0} at ambient temperature is the specified value.

2) The diffusion coefficient is set to kT0 times mobility. The diffusion coefficient and mobility are independent of temperature.

3) The optical absorption constant α(λ) of a layer with band gap *E*g is given by:

$$\alpha(\lambda) = \left(A + \frac{B}{h\nu}\right)\sqrt{h\nu - E_g} \quad \text{(III.11)}$$

Where *hv* is the energy of the photon, and A and B are constants defined.

If the user presses the button (default 1), he can define the properties of (SRH) recombination in the charge layer of the semiconductor. The defect can be removed by clicking the right mouse button on the defect button to be cleared and choosing the (remove) button.

II.2.5. Defects and recombination

1) The "neutral defect" is an idealization of a defect that contributes to (RSH) recombination but does not contribute to the space charge region. In the case of a (neutral fault), only the product □ and Nt affects the solutions dc and ac (through the lifetimes of the carrier; n for example is given by 1/(□n.Nt.vth)): in this case, the centers of the defect contribute to recombination but not at the space charge zone.

2) The lifetime is displayed only when there is a single level of the defect, uniform in space.

3) All parameters in the default menu are assumed to be temperature independent.

4) The user must specify the recombination somewhere, at least in one place (in a layer or at an interface). If it does not do so, a failure of convergence will result in non-equilibrium conditions (non-zero voltage, and/or illumination).

Table II.1: Some defects properties. Depending on the nature of the energy distribution (some parameters have different meanings as seen in Table II.2).

Properties	Description	Value	By default	Unit
Kind	type of defect	-giver -acceptor -natural	Natural	
Sigma n	Cross section electron capture	Digital	1.0E-15	cm2
Sigma_p	Capturing cross section of hole	Digital	1.0E-15	cm^2
Distribution Energy	Fault distribution type	-alone -Uniform -cb vb tail -gauss	Alone	
And	trap energy level respect with the valence band	Digital	0.5	eV
Ekar	Energy characteristic	Digital	0	eV

Profile	Special variation of defect density	-constant -Linear -Exponential	constant	
Lkar	Length characteristic	Digital	0.1	□m
Nleft	max. Defect concentration for layer rightness	Digital	1.0E+14	/cm3 Or /cm3.eV
Nright	max. Defect concentration for the left of the layer	Digital	1.0E+14	/cm3 /cm3.eV

Table II.1: Equidistant energies.

Energy distribution	**Alone**	**Uniform**	**Valencia Band Cue**	**Conduction band tail**	**Gauss**
And	Energy levels	Energy distribution	bottom of the tail	the top of the tail	Energy distribution
Ekar	no meaning	total width of distribution	the characteristic energy (the axis energy)	the characteristic energy (the axis energy)	total width of distribution
Nleft, Nright	density in /cm3	Density distribution constant in /cm3eV	Density distribution constant E=Et in /cm3eV	Constant density distribution in E=Et in /cm3eV	Density distribution constant E=Et on /cm3Ev

Table II.2 : Energy distribution of some defects [4] For each fault distribution an energy axis is calculated with 41 equidistant energies, as:

Distribution Type	The range of energy since	Until	*N(E)* =
Uniform	**And**– Ekar/2	**And**+Ekar/2	*NOT*
vb tail	**And**	**And**+ 7.Ekar	*NOT.*exp(- (E-Et)/Ekar)
cb tail	**And**	**And**- 7.Ekar	*NOT.*exp(- (Et-E)/Ekar)
Gauss	**And**- 3.Ekar	**And**+ 3.Ekar	*NOT.*exp(- ((E-Et) / Ekar)2)

The concentration N in the table above is calculated from Nleft, Nright and Lkar, as:

Table II.4: The concentration N(x).

Spatial profile	*N(x)* =	Noticed
Constant	**Nleft**	**Nright**and Lkar are ignored
Linear	**Nleft**+ *(***Nright**-**Nleft***).(x-x0)/***d**	**Lkar**is ignored
Exponential	*HAS.*exp((x-x0)/Lkar) + B	*HAS*and B are calculated as N(x0) = Nleft and *N(x0+***d***)* =**Nright**

Here the x0 is the spatial coordinate of the left side of the layer, and x0+d that of the right side. If, in the case of an exponential profile, no value for Lkar is specified, an equal defect concentration to 0 will be assumed.

When all the parameters are set, you can add the layer with all its properties to the already existing structure by pressing the "accept" button.

II.2.6. Interface between layers

Between two layered poses we can define the characteristics of the interface by clicking on the right of the rectangle of two layers. Another 3 possible faults can be set by clicking the "defect1,2,3" button.

When the structure is completely defined, the definition file can be saved by clicking the "Save button". When the "OK button" is clicked the energy band panel is shown with different graphics (Figure II.4).

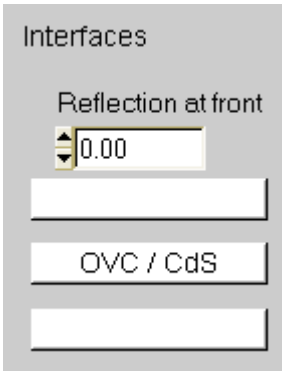

Figure II.4: The interface between the layers.

Tableau II.3 : Some defects properties and the interface between the layers.

Name	Description	Value	Default	Unit
Kind	Fault type	Giver acceptor natural	Natural	
Sigma_n	Electron cross-section capture of the conduction band	Digital	1.0E-15	cm2
Sigma_p	Capturing cross section hole of valence band	Digital	1.0E-15	cm2
Energy **Distribution**	Fault description type	Single Uniform tail cb vb gauss	Single	
And	trap energy level respect with the valence band	Digital	0.5	eV
Ekar	Energy characteristic	Digital	0	eV
NOT	max. Defect concentration	Digital	0	/cm2 gold/cm2.eV

Remarks

1) The energy parameters have the same meaning as in the last section.

2) The interface recombination velocities Sn = $N_i \square_n v_{th,n}$ et $S_p = N_i \square_p v_{th,p}$ are shown only when there is a single energy level interface state. When the thermal velocities of the two-layer formations at the interface have different values, there are different values for the interface recombination velocities of carriers coming from the left or the right.

3) If not explicitly stated otherwise, all parameters of the semiconductor layers and interfaces are assumed to be independent on temperature.

4) The model for interface transport is thermionic emission. The thermal velocity of the transport interface equals the smaller thermal velocity of the two neighboring layers.

5) Reflection of photons at interfaces is not taken into consideration.

II.2.7. Front Contact

The front contact is specified in the same way as the rear contact.

II.3. Numerical parameters

Some numerical parameters are also made available in the user interface by the (numeric) button in the solar cell definition panel: the maximum number of iterations, and clamp values for the electrostatic capacitance and for both quasi-Fermi capabilities. These capacities are not allowed to vary in step by more than the corresponding clamp value during numerical integration. Put these parameter influences on the behavior of convergence in extreme cases where convergence is difficult to obtain. The Figure II.5 presents the numerical parameter window.

II.3.1. Loading and changing an Existing Definition File

To load an already existing definition file, click on the "File button" in the Calculate New menu. In this screen the user can view and select their definition file. If he presses the "OK button" he gets to the energy band panel with balance graphics immediately. Return to the action panel, click on the "action button.

If we want to create a new definition file based on an old one, we must click the "create new" button in the calculate new menu as for a new definition file. In this screen the "Load button" allows one to load an existing definition file one after another one can change it as a new definition file.

If the user clicks the 'edit' button in 'calculate new' menu, he can make changes in the properties of his structure in the same way as he defined the properties by making the definition file.

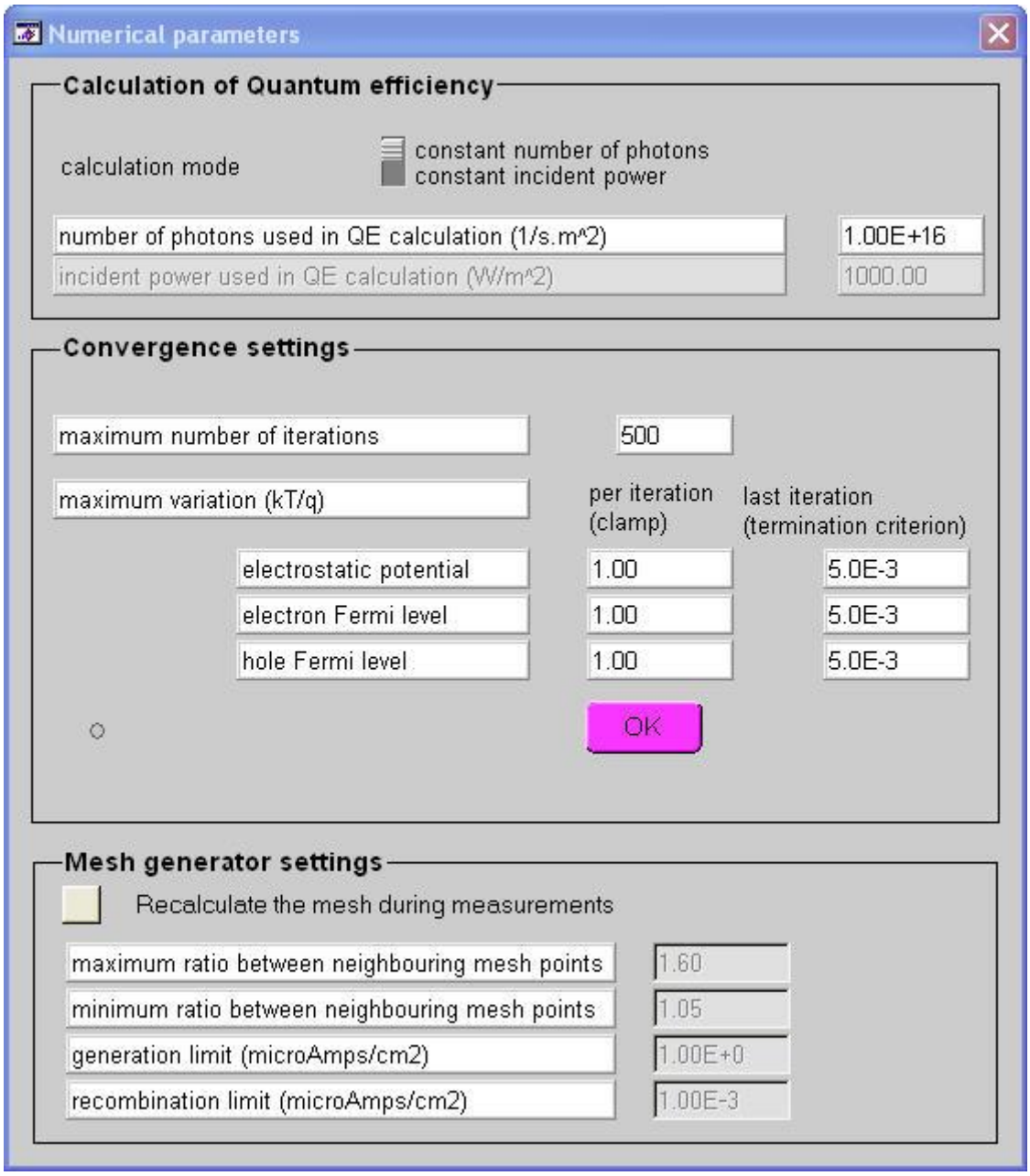

Figure II.5: Numerical parameter window.

II.3.2. Spectrum File

The figure II.6 presents the illumination organization space. We start to select the dark or light mode and in turn from n-side or p-side, contrary we can select spectrum cut off.

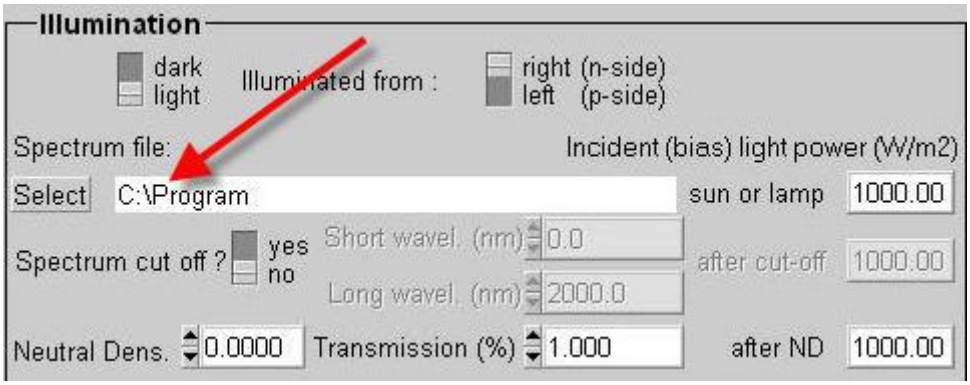

Figure II.6: Illumination organization space

C:\SCAPS\AM1_5G.spe: AM1.5 global spectrum

C:\SCAPS\AM1_5D.spe: AM1.5 direct spectrum

Other spectrum files can be user defined. The spectrum file is an ASCI - files. The first line contains the number of wavelengths that appear in the spectrum file. This row is followed by two columns immediately. The first column specifies the wavelength □ (nm), the second column contains the power of the incident light W (Watt/m^2) in an interval of the wavelength around □ (the number of photons ' wavelength incidents between □-*d*□/2 et □+*d*□/2 is set equal to 5.035 × 10^{15} *W* □ *d*□. The maximum number of wavelengths that appear in the spectrum file is 100 mW/cm^2.

II.3.3. Importing digital simulations

The problem is in the problem definition file. The requested calculations are put in the action "list" in the action panel (see below). After creating, editing or loading a problem definition file, you can return to the action panel. When "cancel" is pressed, no calculation is performed, but the edited cell structure stays in active memory. When "OK" is pressed, the calculation of the defined problem is imported immediately, and the energy band "panel" is displayed. You can return to the action panel by pressing the action button.

Figure II.7 presents the .def file export tool when we can export the previous defined programs or some example programs.

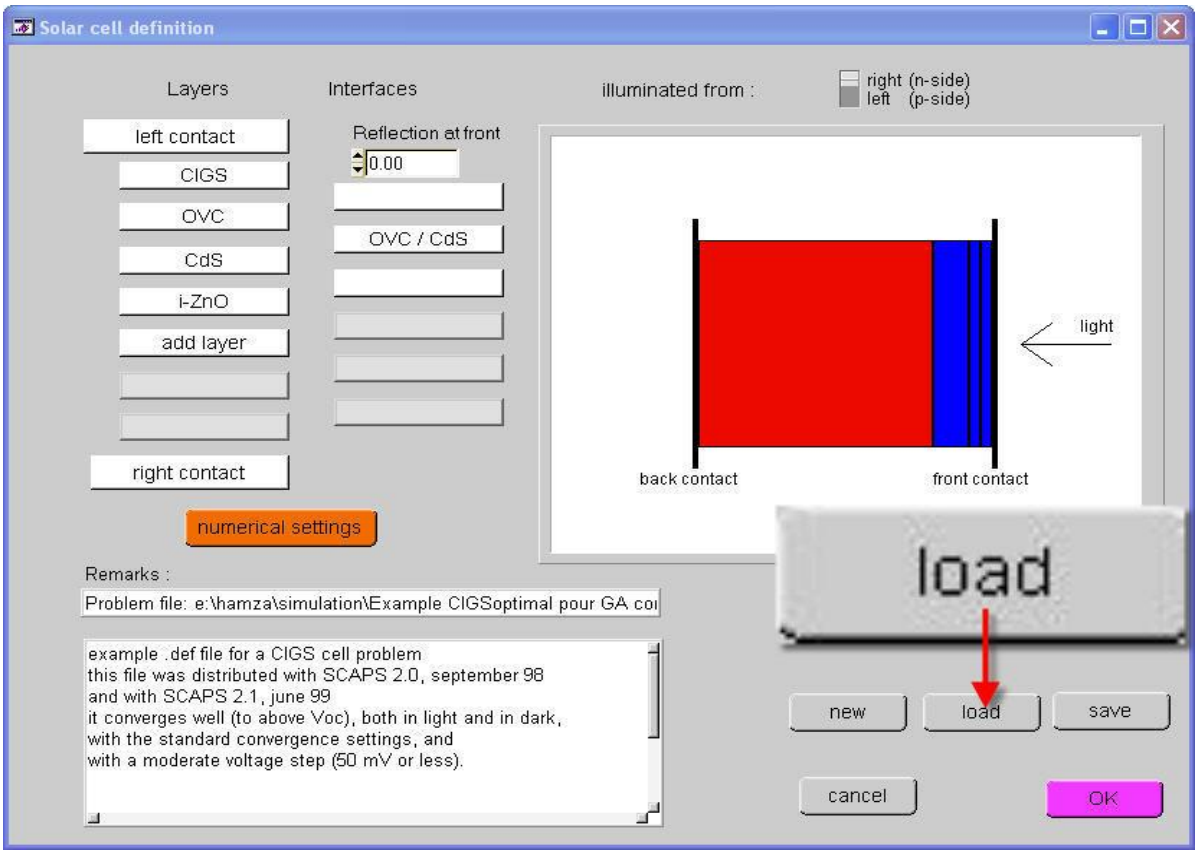

Figure II.7: The .def file export tool.

The action panel allows as to specify an operating point defined by temperature (K), DC voltage (V), illumination conditions (dark spectrum, full spectrum, natural density and/or bandpass filter) and an ac frequency, as seen in Figure II.8.

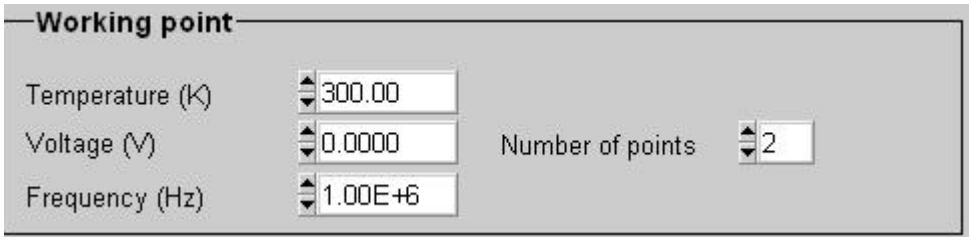

Figure II.8: Operating point determination space.

The spectrum stop option simulates the use of a long bandpass filter and a long stop filter in the DC-illumination condition. This option is effective only when Spectrum Off is set to yes, and when Illumination is on (i.e. "dark" = none). Spectrum stopping affects all calculated curves (although many cell types are not very sensitive to it).

However, the spectral response does not fall to zero in regions where the spectrum is dead. The spectral stop affects the condition of the applied illumination (influence dc, the light source), while the spectral response is calculated as the response to a small source of light from

the ac, superimposed on the light from the bias (simulate the measurement installed with chopped light of a monochromatic and applied light).

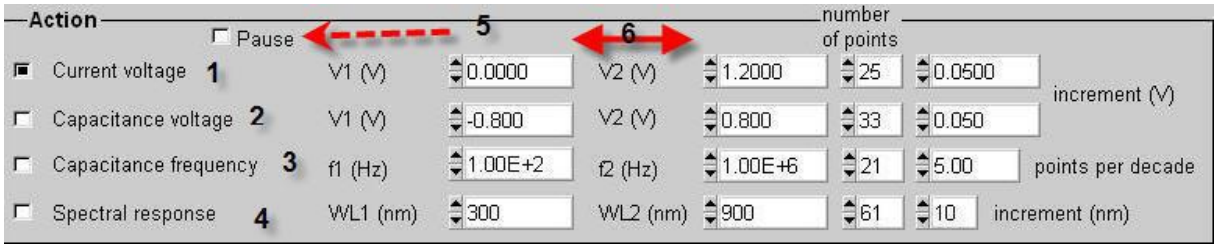

Figure II.9: Parameter adjustment space.

Using the parameters adjustment space, presented in Figure II.9, the following characteristics can be calculated:

1) Current versus Voltage (I-V characteristic): from a specified voltage V1 to V2 (V) in steps n, for the illumination conditions and temperature specified in the operating point (wp).

2) Capacitance against voltage (C-V curves): from a specified voltage V1 to V2 (V) in step n, for the conditions of illumination, temperature and ac frequency, specified in the operating point (wp).

3) Capacitance versus frequency (C-V curves): from a specified frequency f1 to f2 (kHz) in steps n (equidistant on a logarithmic scale) for illumination conditions, the dc influence voltage and temperature specified in the active point.

4) Quantum efficiency QE versus wavelength: from a specified wavelength 1 to 2 (nm) in steps n for the (biased) illumination conditions, the DCs influence voltage and operating point temperature.

Each new calculation begins with the calculation of the equilibrium band diagram (V=0, dark); If the operating point specifies illumination, next the band diagram of the short circuit is calculated. Each next calculation starts from the previously calculated solution. The order of calculation is: first the operating point, then IV, CV, Cf and QE curves, if requested. When the pause button shown in the figure above with arrow numbered 5) in the action panel is enabled, the program stops after each calculation, and resumes when the (continue) button is pressed in the action panel action or in the energy bands panel. When (pause) is turned off, all required calculations are executed one after the other.

Convergence problems can occur when the operating point voltage is too different from zero (= the previously balanced voltage and perhaps Jsc calculation) (see Figure II.10). To overcome this problem, SCAPS allows specifying several steps to be taken to evolve from zero voltage to the operating point voltage. Problems can also occur if the initial calculated IV or CV voltage is too different from the operating point voltage. In this case we can put the influences of the dc voltage equal to the operating point at the starting point of the calculated IV or CV, so that the calculations of IV or CV can start with the correct solution.

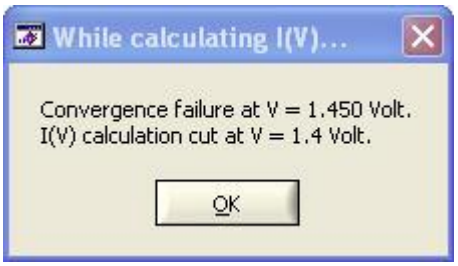

Figure II.10: Convergence failure window.

Once a calculation is finished, it is possible to consider the corresponding IV, CVS, Cf and QE panels. The most recently calculated energy band diagram panel shows. If a Cf calculation is made, SCAPS automatically shows the AC panel.

By pressing the calculate button in the action panel, a new calculation with the same definition file, but with a different action list can be done. If the operating point is the same as for the previous calculation, short circuit and influence of balance conditions will not be recalculated.

II.4. The Action Panel

The Figure II.10 presents the action panel. In this panel the following pieces of information are available:

- The definition of the active point (see above);
- The definition of the action list (see above);
- Set calculation mode: "take a break" between calculations or not (see above);
- Put the problem definition: the "calculate new" button (see above);
- Carry calculations from a new action list: the "calculate next" button (see above);
- "continue" to calculate next action list operation, when "pause" is allowed

- "stop" to stop a calculation that is carried from outside;
- "clear previous" clear previously calculated graphs;
- "graphs" activate the energy bands panel from which in turn we can navigate to all the other graphic panels (IV, CV, Cf and QE).

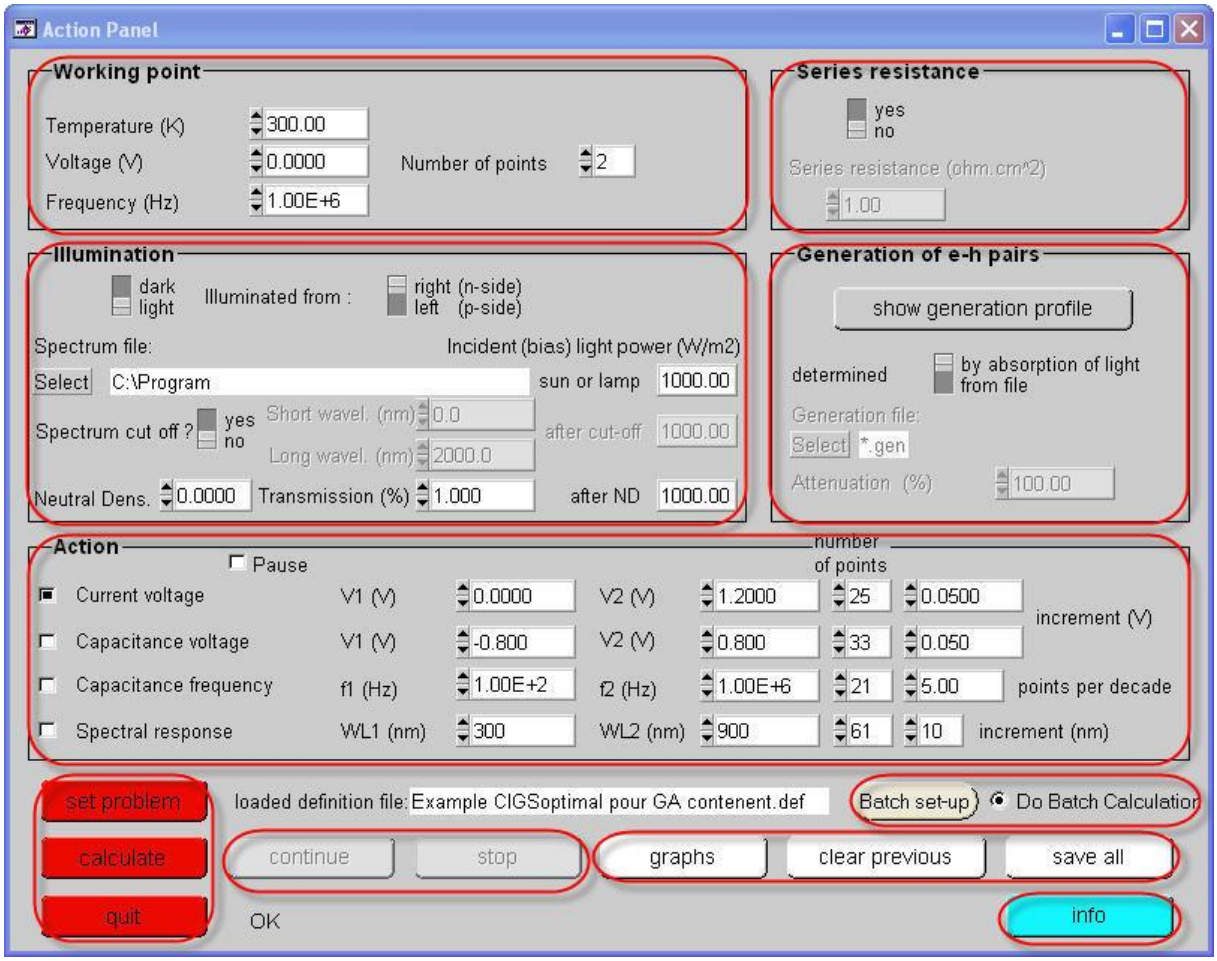

Figure II.11: The Action panel.

- "save all" to always save the results of all preformed calculations in a text file; The data in the text file is separated by labels, and can be cut and can be pasted into an extent sheet or graphics program;
- "exit" exit from SCAPS-1D. This is the only correct way to leave SCAPS!

II.5. Energy band panel

The Figure II.12 presents the energy band panel. In this panel the following buttons are available:

- "continue": resume a calculation stopped by the pause option;

- "save": save the energy band calculation results to a text file;
- "plotter": plot the content of the panel to the Windows default printer. Note: this is a low "quality footprint" screen, only for consideration and purposes of discussion. For presentation purposes, it is best to save the calculation in a text file, and use this file to make presentation graphics with the preferred graphics program;
- "action": return to the action panel.

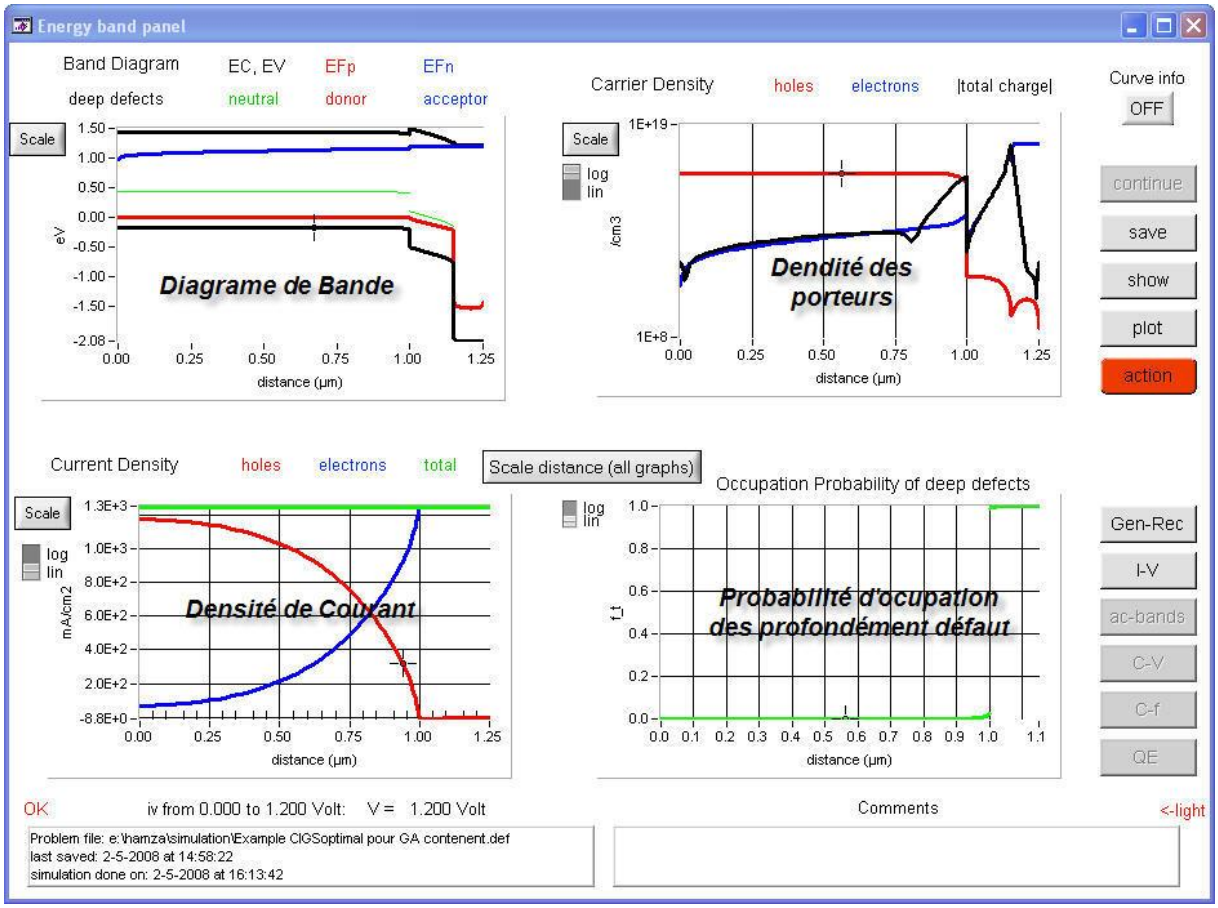

Figure II.12: The energy band panel.

The buttons " **IV**□", **QE**□ ", **AC**□", **CV**□ " et " **Cf**□", navigate to the indicated graphic panels.

The results of the last calculation of the energy band are shown in four graphs: it is therefore in the illumination and the voltage conditions of the last calculation executed (therefore the active point or the last point of IV, QE,… curves).

There is a cursor utility available in the EB - Panel, and in the other graphics panels too. If you click with the mouse on a point of the graph of your choice you can see the x and y

evaluation of that point in the two small windows in the middle of the screen. The units are the same as the user's units of the axes of the relevant graph.

The first graph (upper left) is the show of the (DC) band diagram: black for conduction and valence line, blue for fermi level of electron, red for fermi level of hole or only red if the fermi levels coincide. The fault levels, if present, also have their color: green for a neutral fault, blue for an acceptor type fault and red for a donor type fault. (in fact, the characteristic energy Ekar of defects is shown). It is easy to discern between defect levels and fermi levels, since defect levels exactly follow the sharp band, while fermi levels do not.

The second graph (upper right) shows the carrier densities as a function of distance: blue for electrons, red for holes, and black for total charge.

The third graph (lower left) is the showing of the current density as a function of distance: blue for electrons, red for holes, and green for total current.

The fourth graph (lower right) shows the probability of occupancy of defects as a function of distance: green for neutral defects, blue for acceptor type, red for donor type defects.

II.6. Panel of IV characteristics

The “continue”, “show”, “plot” and “action” buttons, and the navigation button navigation **“EB□”**, **“QE□”, “AC□”, “CV□”** et **“Cf□”** have the same meaning as in the energy bands panel (see Figure II.13).

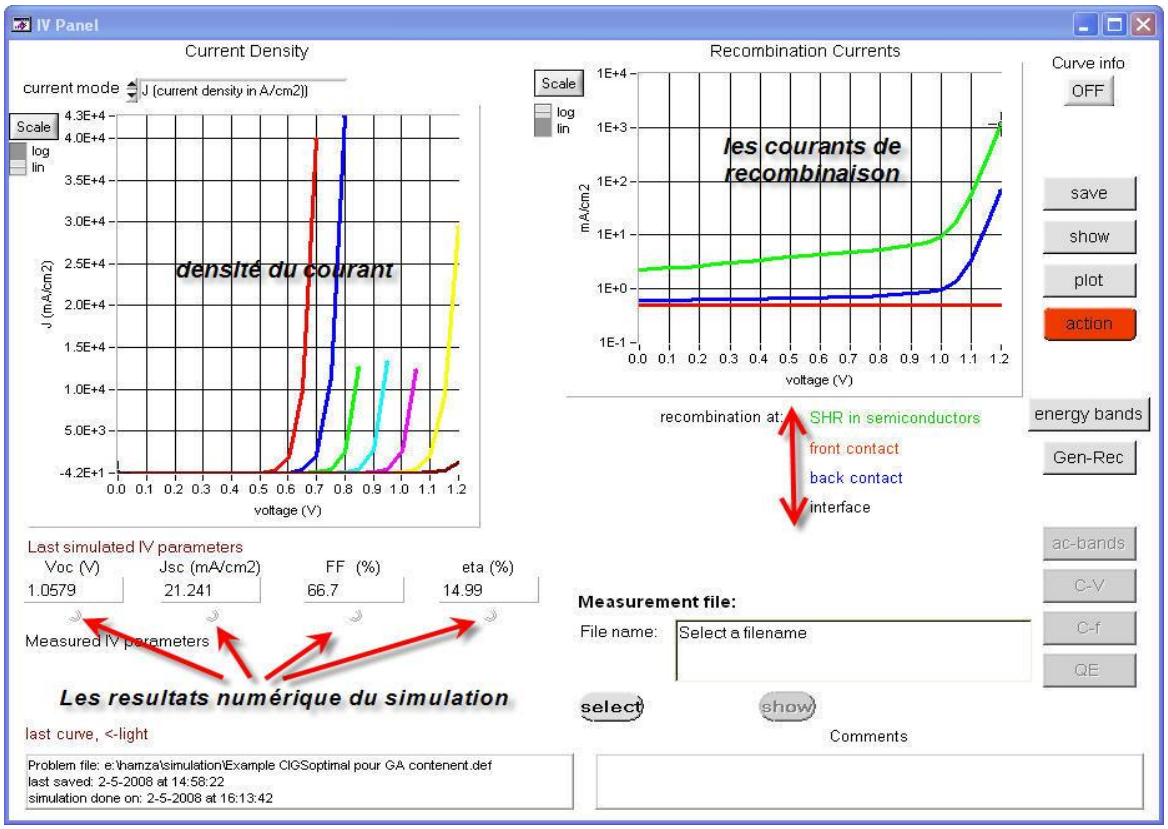

Figure II.13: Panel of JV characteristics.

The “continue”, “show”, “plot” and “action” buttons, and the navigation buttons and **“EB□”, “QE□”, “AC□”, “CV□”** et **“Cf□”** buttons have the same meaning as in the energy bands panel.

The first graph (left) is the exposition of the current density as a function of the applied voltage. The first calculation (that is, after "calculate again", the problem has settled and "OK"), the IV curve (when calculated) is plotted in red. Each next calculation (so after a "calculate next" or after another "calculate again"), a new IV - curve is added (when calculated), in a different color. The color order is: red, blue, green, cyan, magenta, yellow … (14 colors). When "Previous Clear" is pressed on the Action panel, all IV curves are cleared, and the color starts again from red. The second graph (right) is the exposure of the recombination current as a function of the applied voltage:

The new utilities on SCAPS are:

❖ **Batch calculation**

If you want to know the influence of one or more parameters on the solar cell characteristics, using this new option does it easily, it just involves clicking on the Batch button and setting the parameters you want to vary. Variations can be simultaneously made. The Figure

II.13 presents the Batch tool to do the Batch calculation and the panel to input different material parameters.

We must select the instruction (Do Batch Calculation) to perform the batch calculations.

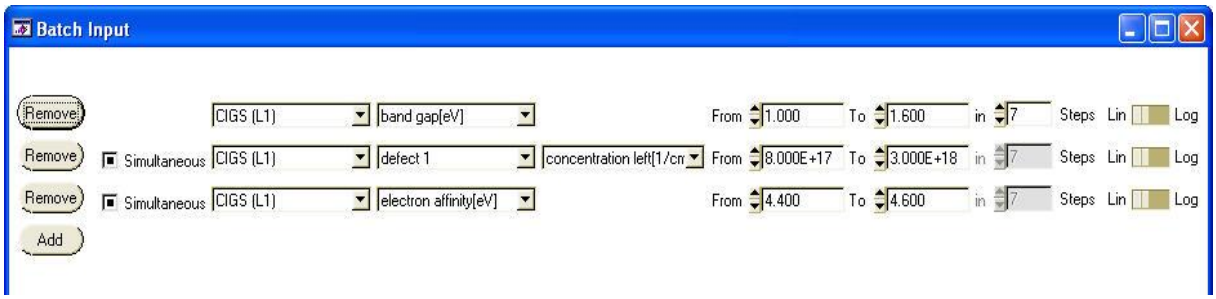

Figure II.14: The Batch tool.

❖ **The Tunnel effect tool**

Currently two tunneling mechanisms are built on SCAPS 2.6 intra band tunneling and tunneling to interface states to put the tunneling option you must click the corresponding button on (the interface states-panel) (see Figure II.15).

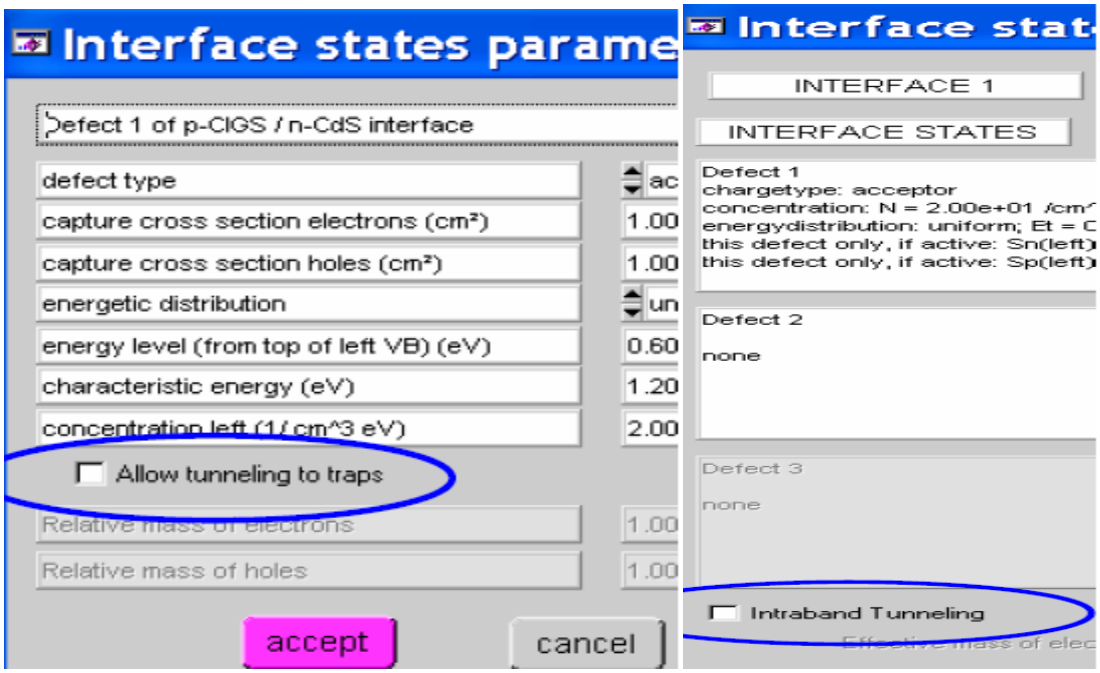

Figure II.15: The tunnel effect tool.

II.7. Conclusion

SCAPS-1D tool, one of the most popular simulators in the world of photovoltaic field simulations, because it is simple and easy for an electronics engineer, who wants to model cells in thin layers of this kind. The results and configurations are valid on a file with a specific extension but accessible in text format and this makes all the operations of (copying, pasting) the results easier, again with the type of data selection being vertical or horizontal.

The possibility of opening several SCAPS-1D windows simultaneously which gives us the power to perform more than one task, depending on the power of the PC and the stability of SCAPS-1D. The latter represents disadvantages for its functionality due to the risk of loss of results. The processing speed is very fast, especially with the new batch tools which allow the user to vary one or more parameters at the same time or separately.

The SCAPS-1D interface is simple but the graphical representation is simpler because the (Zooming) operations are done by hand and also the exploitation of its graphs.

References

[1] A. Niemegeers, S. Gillis et M. Burgelman, 1998. " UN programme de l'utilisateur pour simulation réaliste d'heterojunction du polycrystalline cellules solaires : SCAPS-1D ", Débats de la 2e Conférence Mondiale sur Conversion D'énergie Photovoltaïque (Wien, Österreich, july 1998), pp. 672-675, JRC, Ordre européen,

[2] M. Burgelman, P. Nollet et S. Degrave, semi-conducteur du polycrystalline du 1999. " Modelage cellules " solaires, (a invité) a présenté à la Société de la Recherche des Matières européenne, E-MRS, Strasbourg, France.

[3] A. Niemegeers et M. Burgelman, modelage 1996. " Numérique d'ac caractéristiques de CdTe et CIS cellules " solaires, Proc. 25e IEEE Conférence des Spécialistes Photovoltaïque (D.C. de Washington, april 1996), pp. 901-904, IEEE, Nouveau York,

[4] M. Burgelman, K. Decock, S. Khelifi and A. Abass, (2013). "Advanced electrical stimulation of thin film solar cells", Thin Solid Films, **535** 296-30

[5] K.Decock, P. Zabierowski, M. Burgelman, (2012) "Modeling metastabilities in chalcopyrite-based thin film solar cells", Journal of Applied Physics, 111 043703

Chapter III

Results and discussions

Chapter III: Results and discussions

III.1 Introduction

In the context of the global energy transition and the growing demand for renewable energy sources, solar cells have become increasingly important. Among the various technologies developed, thin-film solar cells-especially those based on the compound $CuIn_{1-x}Ga_xSe_2$ (CIGS)-have attracted significant attention due to their high efficiency, flexibility, and relatively low manufacturing cost [1-4]. However, despite these advantages, improving the performance of these cells remains a technological challenge. The integration of nanostructures such as quantum wells (QD) into the CIGS absorber layer represents a promising solution to broaden the spectral absorption range and enhance charge carrier generation [3-6].

In this work, we study the performance of quantum well solar cells (QDSC) based on CIGS absorber using SCAPS-1D simulator. This simulator is widely used modelling tool in the field of semiconductor photovoltaics [1,7]. The aim is to analyse the impact of introducing quantum wells on key performance parameters such as open-circuit voltage (V_{oc}), short-circuit current density (J_{sc}), Fill factor (*FF*), and overall efficiency (η).

III.2 Presentation of $CuIn_{1-x}Ga_xSe_2$ (CIGS) material

III.2.1 Structure and Composition

$CuIn_{1-x}Ga_xSe_2$ (CIGS) with $0 \leq x \leq 1$ is a direct bandgap semiconductor with a tetragonal chalcopyrite structure. It is an alloy of $CuInSe_2$ (CIS) and $CuGaSe_2$ (CGS), where the variable *x* represents the fraction of gallium (Ga) replacing indium (In) in the crystal lattice:

$$x = \frac{[Ga]}{[Ga+In]} \qquad \text{(III.1)}$$

- When $x = 0$, the material is pure $CuInSe_2$, with a bandgap of around 1.04 eV.
- When $x = 1$, it becomes $CuGaSe_2$, with a larger bandgap of approximately 1.68 eV.
- By tuning the *x* value between 0 and 1, we can precisely control the bandgap, allowing us to tailor the material to optimize solar energy absorption a technique known as bandgap engineering.

This adjustability makes CIGS a highly versatile absorber material for thin-film solar cells.

III.2.2 Advantages of CIGS materials for Solar Cells

CIGS materials offers several outstanding properties that make it ideal for solar energy conversion:

- **Direct bandgap (Eg = 1.07 - 1.7 eV):** Enables efficient light absorption even with very thin layers (1–2 µm).
- **High absorption coefficient:** Efficiently captures visible light, minimizing optical losses.
- **Adjustable bandgap:** Tuning Ga content allows optimization of open-circuit voltage (*V*oc) and short-circuit current (*J*sc).
- **Flexible deposition:** Can be deposited on various substrates (glass, metal, plastic), enabling both rigid and flexible solar modules.
- **Good chemical stability:** Offers excellent resistance to environmental degradation.

III.2.3 General formula of energy gap and affinity of CIGS material

The general formula for the bandgap energy (Eg) and electron affinity (χ) of CIGS (Copper Indium Gallium Diselenide) materials used as absorbers in thin-film solar cells depends on the gallium-to-indium ratio, often expressed as the Ga/(Ga+In) or GGI ratio. The material formula is typically written as:

$$CuIn_{1-x}Ga_xSe_2 \quad (\text{where } 0 \leq x \leq 1) \qquad \text{(III.2)}$$

a) Bandgap Energy (Eg): The bandgap of CIGS varies with the Ga content (*x*) and is typically expressed as:

$$E_g(x) = x.E_{g.CuInSe2} + (1-x).E_{g.CuInSe2} - b.x(1-x) \qquad \text{(III.3)}$$

- $E_{g.CuInSe2} \approx 1.04\ eV$
- $E_{g.CuGaSe2} \approx 1.67\ eV$
- b is the bowing parameter, typically in the range 0.15 – 0.25 eV

So $$E_g(x) = 1.04 + 0.63x - 0.25x(1-x) \qquad \text{(III.4)}$$

b) Electron Affinity (χ):

Electron affinity also varies with composition. A general empirical relation is:

$$\chi(x) = (1-x).\chi_{CuInSe2} + x.\chi_{CuGaSe2} - b_\chi.x(1-x) \qquad \text{(III.5)}$$

- $\chi_{CuInSe2} = 4\ eV$
- $\chi_{CuGaSe2} = 4.5\ eV$
- b_χ (bowing for electron affinity) ≈ 0.08 eV (approximate, not always considered).

So: $$\chi(x) = 4.6 - 0.4x - 0.08.x(1-x) \quad \text{(III.6)}$$

These relations [8-11] allow you to estimate the material's band alignment and suitability in heterojunction solar cells. The Figure III.1 shows the calculated values of the bandgap energy and the corresponding electron affinity of CIGS material:

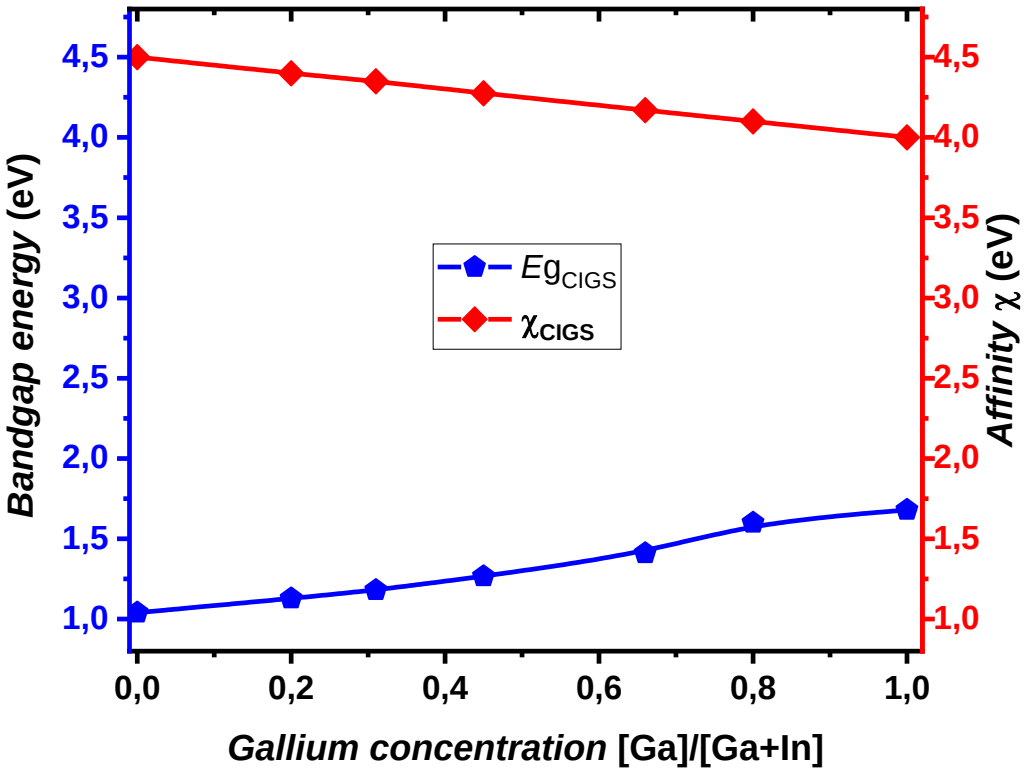

Figure III.1: Variation of bandgap energy and affinity of Cu (In,Ga)Se_2 material as a function of Gallium concentration *x*.

III.3 Numerical study of substrate CIGS solar cell

III.3.1 Substrate CIGS structure

The conventional structure of CIGS solar cell consists of a glass substrate, a molybdenum back contact layer, a CIGS absorber layer, a CdS buffer layer and finally a transparent

conducting oxide front contact ZnO layer. This structure is designed to optimize light absorption, charge transport, and collection in CIGS absorber layer.

In the conventional structure, the n-type CdS buffer layer is inserted between the ZnO window layer and p-type CIGS absorber layer to make a high-quality p-n junction in the interface. The n-type CdS buffer layer was taken using 0.1 nm-thick and 2×10^{17} cm^{-3} donor density with a gap of 2.4 eV. The CIGS absorber layer is a p-type semiconductor with 3 µm-thick and 2×10^{16} cm^{-3} acceptor density with a moderate gap E_g = 1.04 eV and E_g = 1.67 eV. The degenerate ZnO(n+) window layer was taken as a wide band-gap Transparent Conducting Oxide (TCO) semiconductor (3.30 eV), with 0.1 nm-thick and 1×10^{19} cm^{-3} donor density. In the proposed structures, a schematic view of the conventional CIGS solar cell structure is displayed in Figure III.2.

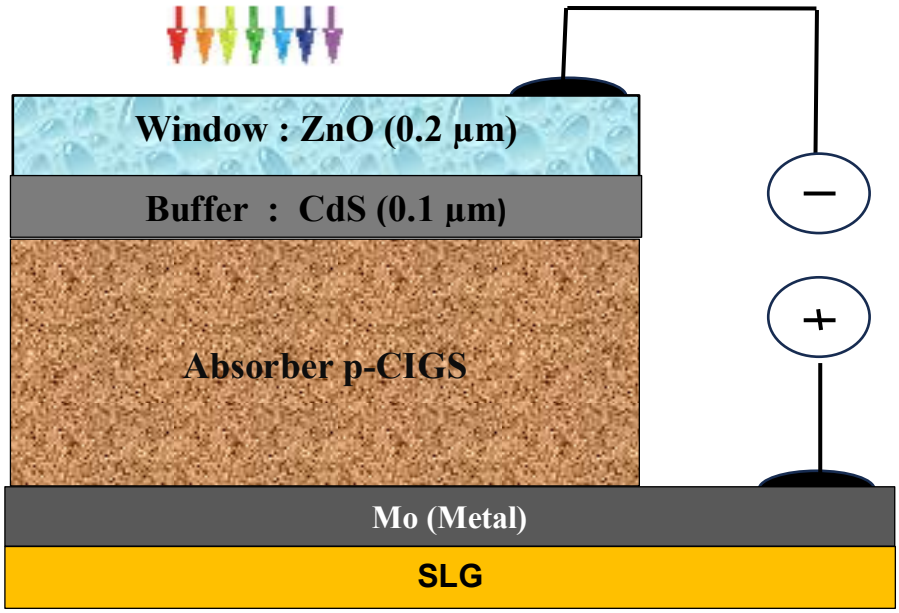

Figure III.2: CIGS solar cell structures

III.3.2 SCAPS-1D input parameters for conventional CIGS/CdS/ZnO solar cell (Substrate Configuration)

As we mentioned above, the SCAPS-1D simulator allows the solution of a set of basic semiconductor equations consisting of the Poisson equation and the continuity and transport equations for electrons and holes [7], the Newton method was selected for solving the basic

semiconductor equations in the software as a default method. The band-gap E_g of CIGS alloys was calculated using the data mentioned in Table III.1 [8-11].

Table III.1: Parameters values ZnO and CdS and CIGS solar cell structures used in SCAPS-1D

Material properties	ZnO	CdS	CIGS
Thickness [µm]	0.2	0.1	2
Band gap [eV]	3.30	2.40	1.68
Electron affinity [eV]	4.45	4.20	4.00
Dielectric permittivity (relative)	9	10	13.6
CB (conduction band) effective density of states [cm^{-3}]	2.2×10^{18}	2×10^{18}	2.2×10^{18}
VB (valence band) effective density of states [$1/cm^3$]	1.8×10^{19}	1.8×10^{19}	1.8×10^{19}
Electron mobility µn [cm^2 /Vs]	100	100	100
Hole mobility µp [cm^2 /Vs]	250	250	250
Shallow uniform donor density N_D [$1/cm^3$]	1×10^{18}	1×10^{17}	10
Shallow uniform acceptor density N_A [$1/cm^3$]	0	0	2×10^{16}

In the first part of this work, we will study the effect of CIGS layer thicknesses and doping concentration on the current density-voltage (*J-V*) characteristics and quantum efficiency (QE) of the conventional cell ZnO/CdS/CIGS structure. Figure III.3 presents the absorption coefficient curves for CIGS materials with different Gallium fractions (*x*). These curves were extracted from the SCAPS database [7].

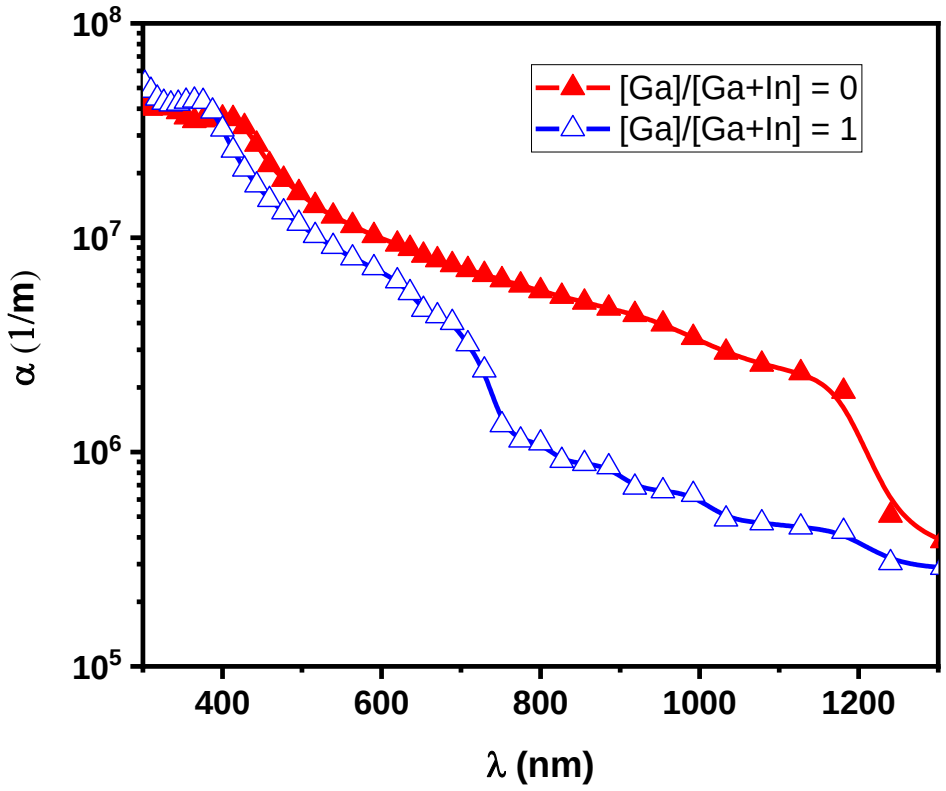

Figure III.3: Absorption coeffficient as a function of wavelength for CIGS materials.

III.4 Effect of Gallium Concentration on CIGS Solar Cell Performance

The figure III.4 presents the evolution of key photovoltaic parameters—open-circuit voltage (V_{OC}), short-circuit current density (J_{sc}), fill factor (*FF*), and conversion efficiency (η)—as a function of gallium concentration *x* in the CIGS absorber layer.

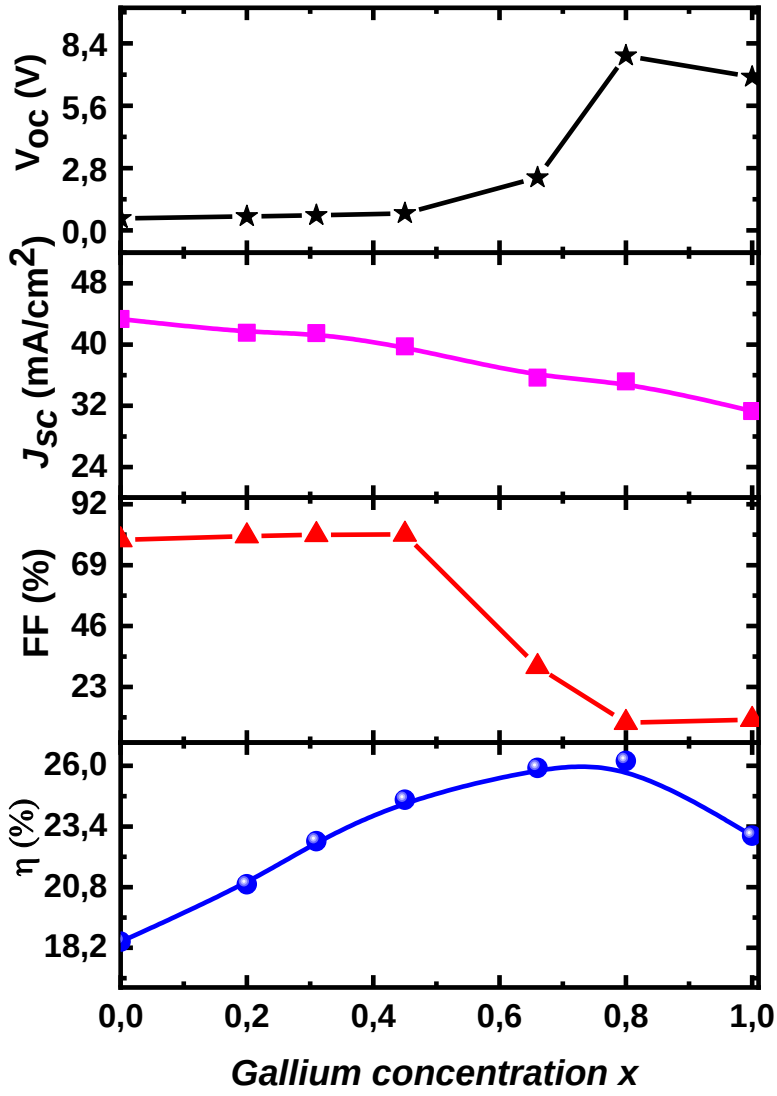

Figure III.4: Effect of Gallium concentration on the photovoltaic performance of substrate CIGS solar cells.

As the gallium content increases, V_{oc} shows a gradual rise, followed by a sharp increase at higher concentrations. This behavior is attributed to the increase in the bandgap of the CIGS alloy with higher gallium content, which reduces intrinsic carrier concentration and improves built-in potential. In contrast, J_{sc} exhibits a decreasing trend with increasing Ga content, likely due to reduced absorption of longer-wavelength photons as the bandgap widens.

The fill factor (*FF*) remains relatively stable up to $x \approx 0.6$, then drops significantly for higher gallium concentrations, possibly due to increased series resistance or interface

recombination effects at higher bandgaps. Consequently, the efficiency (η) initially increases with Ga incorporation and reaches a maximum around $x \approx 0.4–0.6$, where a good balance is achieved between high V_{oc} and acceptable J_{sc}. Beyond this point, the efficiency declines due to the combined effects of decreasing *J*sc and *FF*.

Overall, these results indicate that there is an optimal gallium concentration range—typically around $x = 0.4$ to 0.6—that optimizes the performance of CIGS solar cells by adjusting the bandgap to achieve an improved balance between voltage and current.

III.5 Effect of CIGS thickness on the photovoltaic performance of substrate CIGS solar cell structure

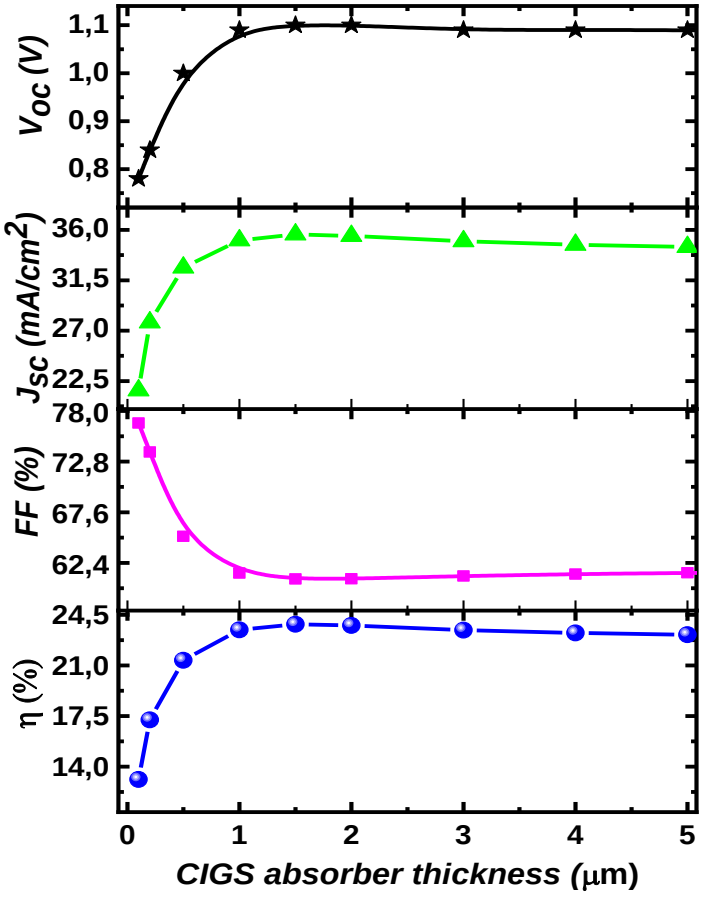

Figure III.5: Cell performance as a function of CIGS absorber layer thickness.

Figure III.5 illustrates the evolution of solar cell performance as a function of the absorber layer thickness. Both V_{oc} and J_{sc} increase rapidly with thickness up to around 2–3 µm, after which they reach a plateau, indicating saturation in light absorption and efficient charge

separation. The fill factor shows a slight initial decrease before stabilizing, likely due to internal resistance effects. The overall efficiency (η) follows a similar trend, increasing quickly for thin layers and then leveling off.

These results suggest that an absorber thickness of about 1 μm is sufficient to achieve optimal performance. This allows for reduced material usage while maintaining high efficiency, which is a significant advantage for developing cost-effective thin-film solar cells.

III.6 Effect of acceptor concentration of CIGS absorber

The Figure III.6 highlights the influence of acceptor doping concentration of CIGS absorber layer, N_A(CIGS) on the performance of a photovoltaic cell by showing the variation of four key parameters: open-circuit voltage (Voc), short-circuit current density (Jsc), fill factor (FF), and power conversion efficiency (η).

For N_A values up to 10^{14} cm^{-3}, the device performance remains stable, indicating that low doping levels do not significantly affect cell behavior. At 10^{15} cm^{-3} a slight increase in (V_{oc}) is observed, likely due to enhanced charge separation resulting from a stronger internal electric field. However, when N_A reaches 10^{16} cm^{-3}, all parameters especially *J*sc, *FF*, and η drop sharply. This degradation is likely caused by increased recombination losses (such as Auger recombination) and impaired carrier collection. Therefore, Figure III.xx clearly shows that excessive acceptor doping negatively impacts solar cell performance, emphasizing the importance of optimizing doping levels to maintain high efficiency.

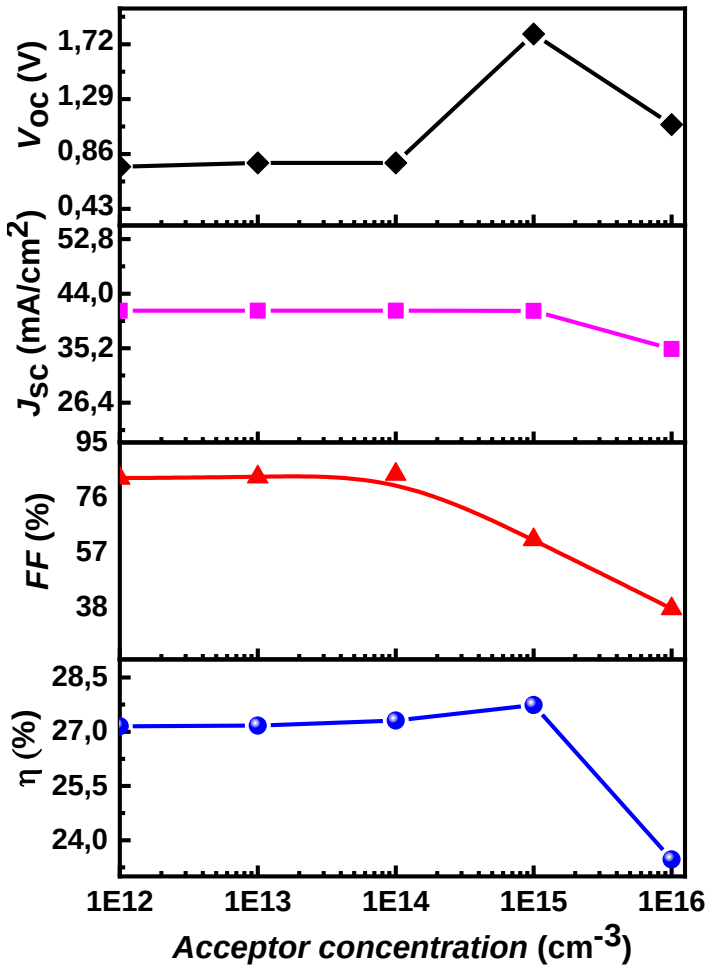

Figure III.6: Variation of solar cell performance as a function of acceptor concentration N_A(CIGS).

III.7 Effect of defect density of CIGS absorber

Figure III.7 presents the effect of increasing defect density (N_t) on the main performance metrics of a CIGS solar cell. As the defect density increases from 10^{13} to 10^{19} cm^{-3}, *V*oc exhibits a sharp decline, especially beyond 10^{15} cm^{-3}. This reduction is attributed to enhanced recombination of charge carriers due to the presence of deep-level defects, which limit the separation of photogenerated carriers and reduce the built-in potential of the junction. *J*sc remains relatively stable across lower defect densities but begins to decrease slightly beyond 10^{17} cm^{-3}. This trend suggests that at high defect levels, carrier lifetime is reduced due to recombination centers, which hinders carrier collection.

The fill factor remains relatively stable throughout the investigated defect density range, indicating that the series and shunt resistance values, as well as the general shape of the current–voltage curve, are not significantly impacted until very high defect concentrations. In contrast, the power conversion efficiency η follows a trend similar to that of *V*oc, maintaining stable values at lower defect densities and declining sharply beyond 10^{13} cm^{-3}. This reduction in efficiency is a direct consequence of the combined degradation in both *V*oc and *J*sc.

In summary, the results demonstrate that low levels of defect density do not significantly impair device performance. However, when the defect density exceeds a critical threshold, particularly beyond 10^{14} cm^{-3}, the photovoltaic parameters—especially *V*oc and η—deteriorate significantly. These findings emphasize the importance of minimizing defect density in the quantum well region to ensure high-efficiency solar cell operation.

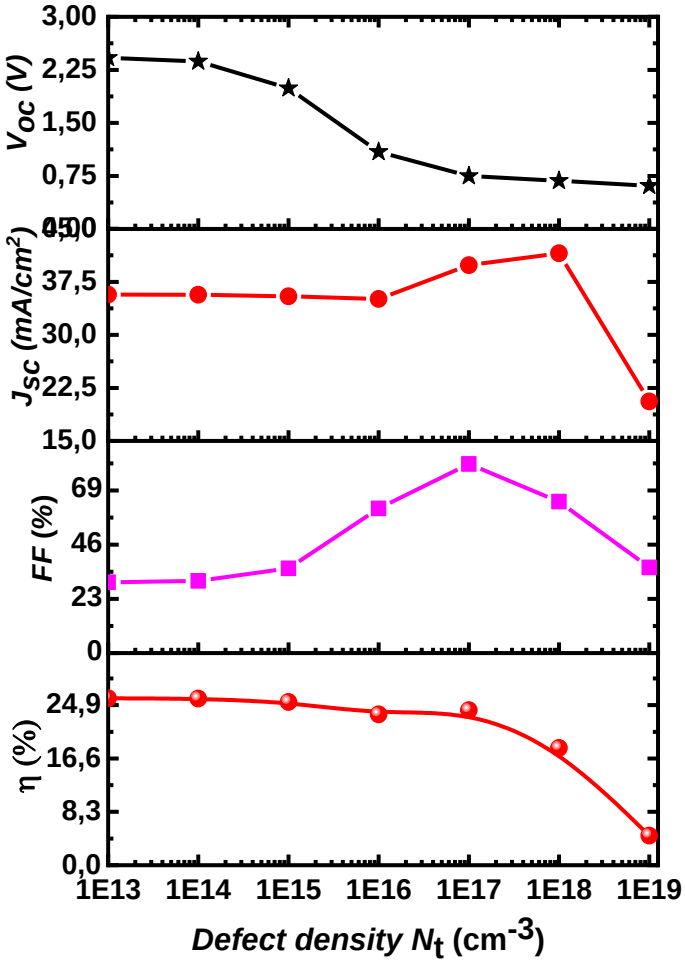

Figure III.7: Effect of defect density of CIGS absorber layer on the solar cell performances.

III.8 Study of substrate Cu(In,Ga)Se_2 Quantum Well Solar Cell (QDSC)

III.8.1 Overview of Quantum Well System

A quantum well is a nanostructure where charge carriers, such as electrons and holes, are confined in one dimension, allowing them to move freely in the other two. This confinement occurs when a thin layer of a low bandgap material is sandwiched between two layers of higher bandgap materials. The resulting potential well leads to quantized energy levels, which can enhance the optical and electronic properties of semiconductor devices.

In solar cells, quantum wells can improve light absorption, carrier collection, and overall efficiency by enabling better control of the band structure and facilitating absorption in a broader range of the solar spectrum. Figure III.8 presents the structure profile and the energy band diagram of the quantum well system.

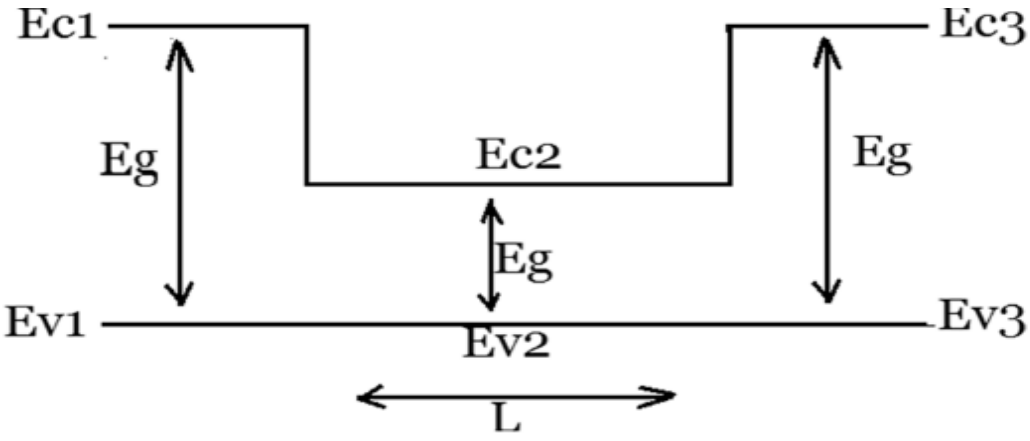

Figure III.8: Structure profile and the energy band diagram of the quantum well system.

III.8.2 Applications of Quantum Well in solar cell structures

Quantum Well solar cells, which utilize advanced quantum well technology, have a wide range of applications due to their high efficiency and ability to perform well under various lighting conditions. They are commonly used in residential and commercial solar panels, providing more electricity even in partial sunlight, which helps reduce energy bills and promote clean energy use.

In space applications, Quantum Well cells are ideal for satellites and spacecraft because they resist cosmic radiation and deliver reliable power in extreme environments. These cells are also found in portable and mobile devices such as solar chargers for phones and laptops, making them perfect for on-the-go energy needs.

In industrial settings, Quantum Well solar cells power autonomous systems like water pumps in rural areas or sensors for the Internet of Things. Finally, they play a significant role in sustainable building designs and smart cities by integrating into building surfaces to generate renewable energy and reduce urban carbon footprints.

III.8.3 Numerical modelling of substrate CIGS solar cell with QW (CIGS QDSC)

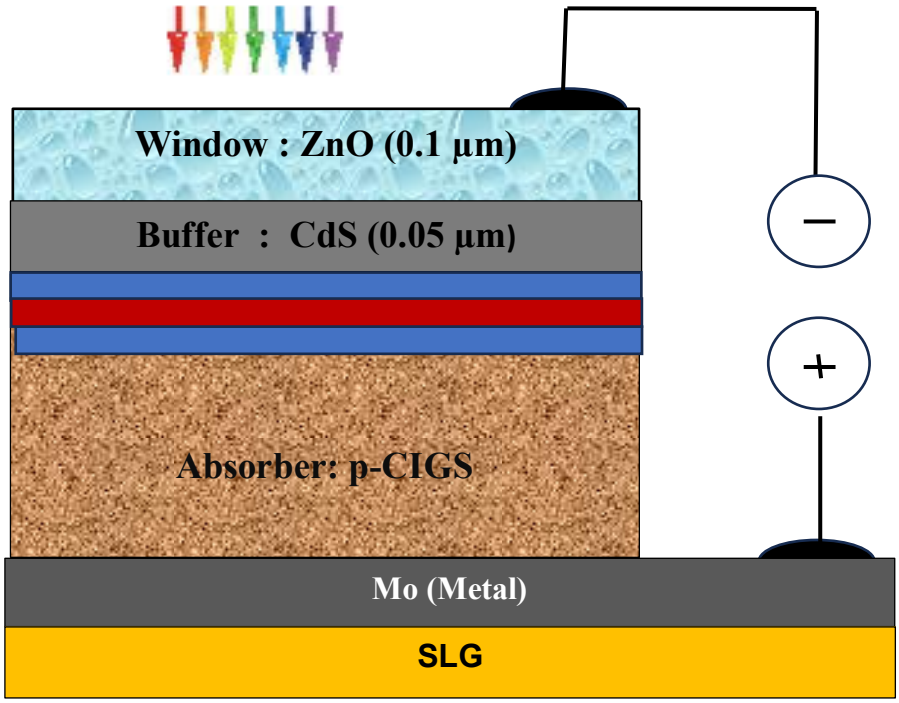

Figure III .9: Cu (In,Ga)Se_2 solar cell structure introducing the quantum well system.

Table III.2: Parameters values of CIGS QWSC used in the simulation.

Material properties	ZnO	CdS	CIGS-barrier	CIGS-Well
Thickness [µm]	0.2	0.1	0.01	0.01
Band gap [eV]	3.30	2.40	1.41	1.18
Electron affinity [eV]	4.45	4.20	4.17	4.35
Dielectric permittivity (relative)	9	10	13.6	13.6
CB (conduction band) effective density of states [cm^{-3}]	2.2×10^{18}	2×10^{18}	2.2×10^{18}	2.2×10^{18}
VB (valence band) effective density of states [cm^{-3}]	1.8×10^{19}	1.8×10^{19}	1.8×10^{19}	1.8×10^{19}
Electron mobility µn [cm^2 /Vs]	100	100	100	100
Hole mobility µp [cm^2 /Vs]	250	250	250	250
Shallow uniform donor density N_D [$1/cm^3$]	1×10^{18}	1×10^{17}	10	10
Shallow uniform acceptor densityN_A [$1/cm^3$]	0	0	2×10^{16}	2×10^{16}

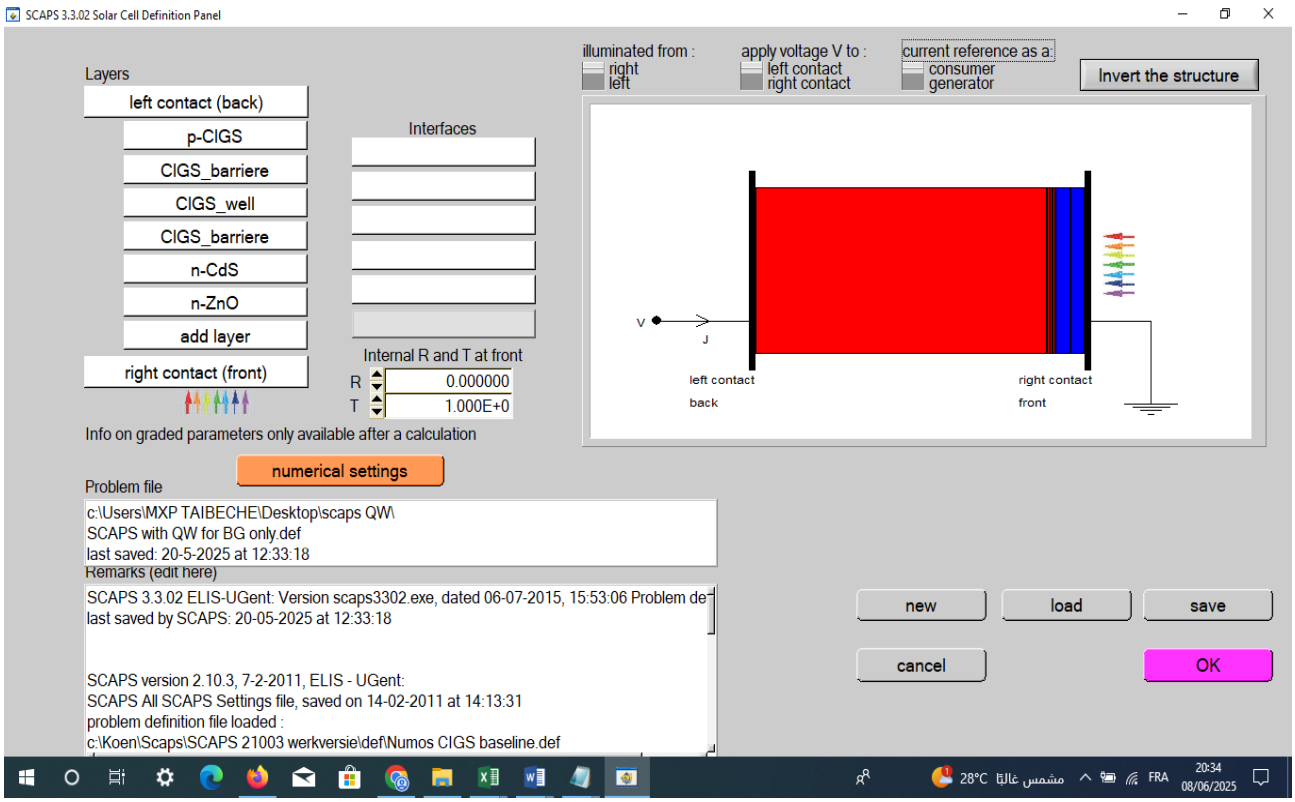

Figure III.10: SCAPS 3302 Solar Cell Definition panel for CIGS SC with QW.

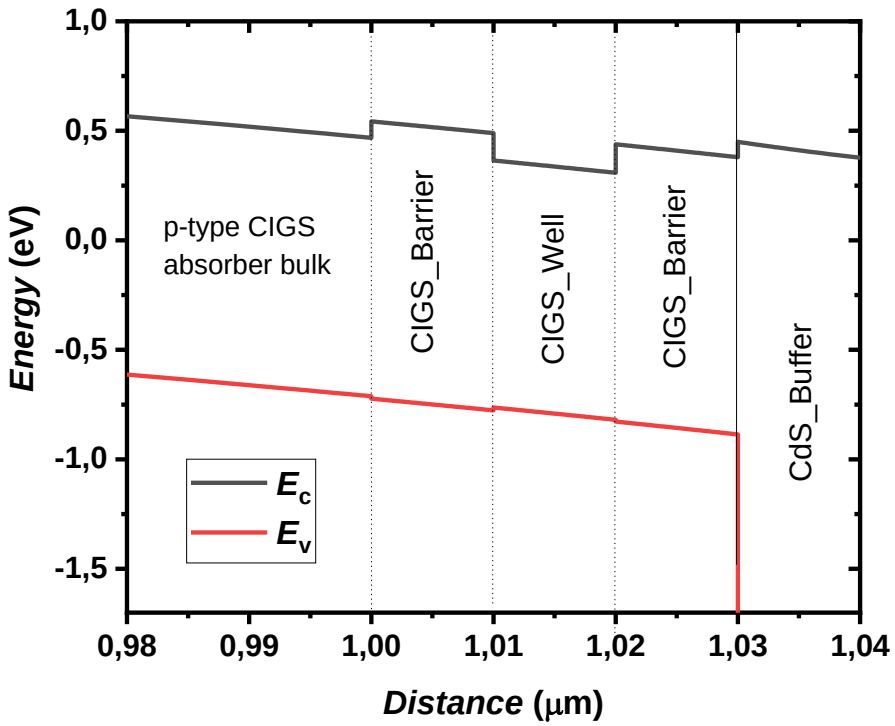

Figure III.11: Energy band profile of a multilayer CIGS-based solar cell structure included the quantum well system.

The Figure III.11 illustrates the energy band profile of a multilayer CIGS-based solar cell structure. It shows the conduction band edge Ec (black line) and the valence band edge Ev (red line) as a function of position across different regions of the device. From left to right, the structure consists of a p-type CIGS absorber bulk, followed by a CIGS barrier, a CIGS quantum well, another CIGS barrier, CdS buffer layer and finally a ZnO window layer. The CIGS-Well is positioned between two CIGS-Barrier layers, forming a quantum well that confines electrons due to the lower energy level of the conduction band in that region.

A significant feature is the conduction band spike at the interface between the CIGS absorber and the CdS buffer, which can act as a barrier to electron transport. The valence band shows a smooth gradient, indicating a built-in electric field that helps in the separation and transport of charge carriers. This energy band diagram is characteristic of advanced CIGS solar cells with quantum well structures, designed to improve light absorption and carrier collection efficiency.

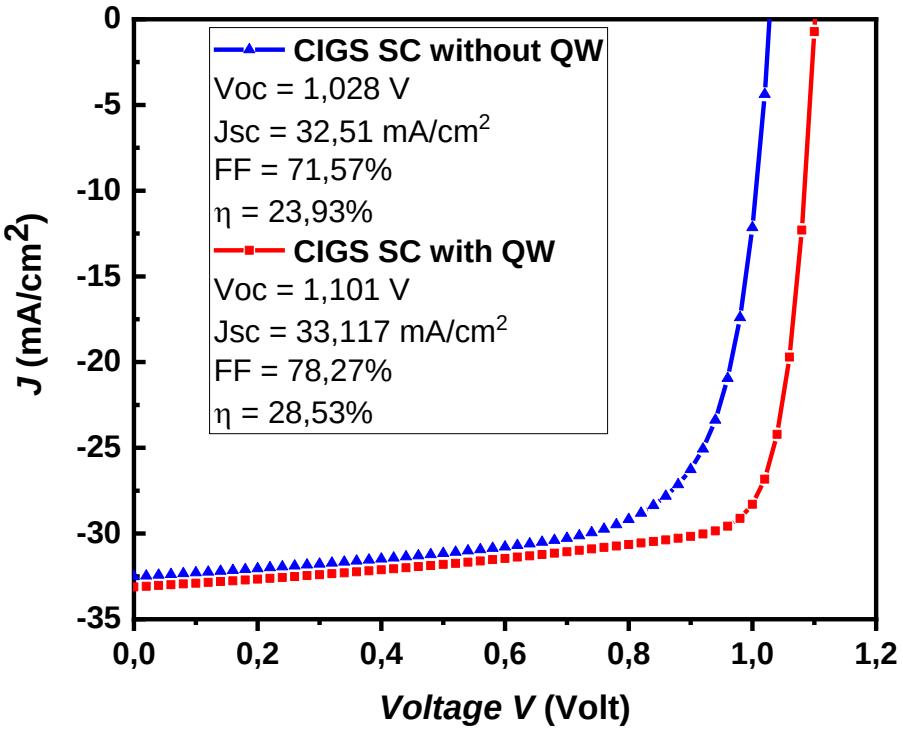

Figure III.12: Current density–Voltage (J–V) characteristics of two CIGS solar cells: one without quantum wells (QW) and one with QW system.

The figure III.12 presents the current density–voltage (J–V) characteristics of two CIGS (Copper Indium Gallium Selenide) solar cells: one without quantum wells (QW) and one with QW. The blue curve represents the solar cell without QW, while the red curve corresponds to the one with QW. The photovoltaic parameters clearly show improved performance with the inclusion of QWs. The open-circuit voltage (Voc) increases from 1.028 V to 1.101 V, indicating better charge separation and reduced recombination. The short-circuit current density (Jsc) also shows a slight improvement, from 32.51 mA/cm² to 33.117 mA/cm², suggesting enhanced light absorption or carrier collection. Moreover, the fill factor (FF) improves from 71.57% to 78.27%, which reflects a better-quality junction and reduced resistive losses. As a result, the overall conversion efficiency (η) increases significantly from 23.93% to 28.53%. These results demonstrate that integrating quantum wells into the CIGS solar cell structure positively impacts all key performance parameters, making them a promising approach for achieving higher efficiency in thin-film solar cells.

III.8.4 Effect of well layer thickness on the performance of CIGS QWSC

The impact of the quantum well layer thickness on the photovoltaic performance parameters is depicted in Figure III.13. As the thickness increases from 0 to 0.1 µm, a notable decrease in the open-circuit voltage (Voc) is observed. This reduction is attributed to enhanced carrier recombination within the thicker well region. As the active layer becomes thicker, the probability of non-radiative recombination events increases, which diminishes the quasi-Fermi level separation and thus lowers Voc. Conversely, the short-circuit current density exhibits a slight but steady increase with increasing well layer thickness. This improvement is likely due to enhanced photon absorption in thicker layers, leading to a greater generation of charge carriers. However, the modest nature of the increase suggests that the benefits of improved absorption are partially offset by recombination losses.

The fill factor (FF) also shows a gradual enhancement across the thickness range. This trend may be linked to improved charge transport and collection efficiency, as well as a more favorable electric field distribution within the device. Such improvements contribute positively to the output characteristics of the solar cell.

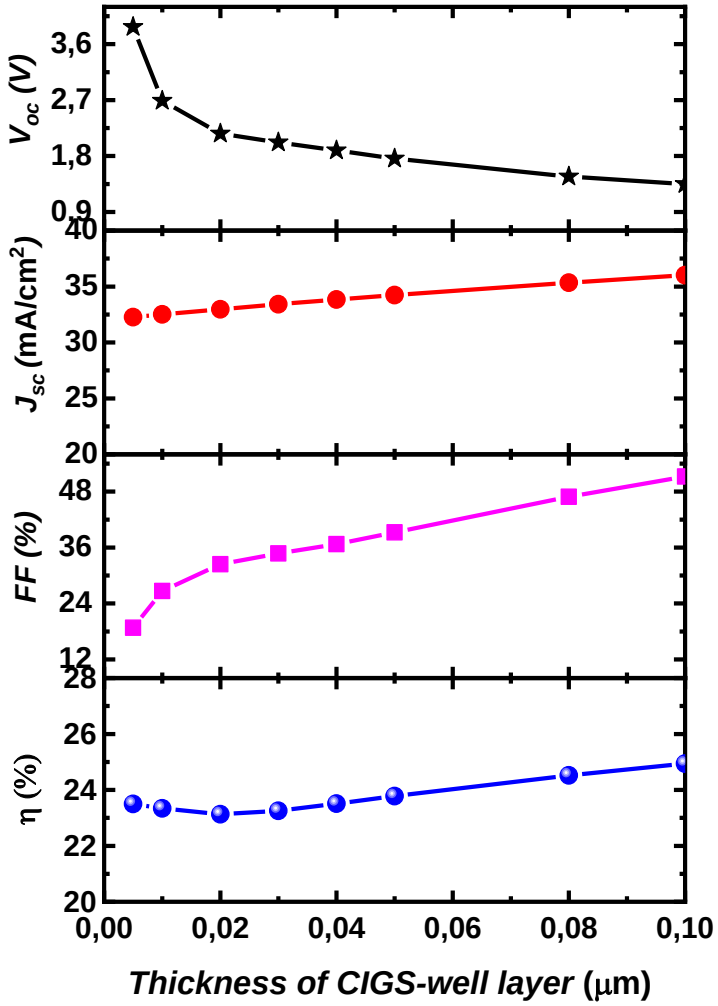

Figure III.13: Effect of the CIGS-well thickness on the performance of CIGS QDSC.

As a result of the combined trends in *J*sc and *FF*, the overall power conversion efficiency (η) increases slightly with increasing well thickness. Although the decreasing *V*oc imposes a limiting factor, the concurrent enhancements in other parameters lead to a net improvement in efficiency. Nevertheless, the efficiency gain is modest, indicating that excessive thickening without addressing recombination could be detrimental. In summary, increasing the well layer thickness enhances light absorption and current generation, while also introducing recombination-related losses. Therefore, optimizing the thickness of the well layer is essential to achieve a balance between these competing effects and to maximize device performance.

III.8.5 Effect of defect concentration of CIGS-well layer

The influence of defect density N_t in the well layer on the photovoltaic performance parameters is illustrated in Figure III.14. As shown, the open-circuit voltage Voc remains nearly constant for defect densities ranging from 1×10^{10} to 1×10^{13} cm^{-3}, beyond which a noticeable decline is observed. This behavior can be attributed to the increased density of recombination centers, which reduce the separation between quasi-Fermi levels, thus lowering *V*oc.

The short-circuit current density *J*sc exhibits a slight enhancement at intermediate defect densities, possibly due to the temporary contribution of shallow traps in aiding carrier collection. However, at higher defect densities, *J*sc decreases due to dominant non-radiative recombination mechanisms that limit carrier lifetime and collection efficiency.

The fill factor (*FF*) remains relatively stable throughout the investigated defect density range, indicating that the series and shunt resistance values, as well as the general shape of the current–voltage curve, are not significantly impacted until very high defect concentrations. In contrast, the power conversion efficiency η follows a trend similar to that of *V*oc, maintaining stable values at lower defect densities and declining sharply beyond 10^{13} cm^{-3}. This reduction in efficiency is a direct consequence of the combined degradation in both *V*oc and *J*sc.

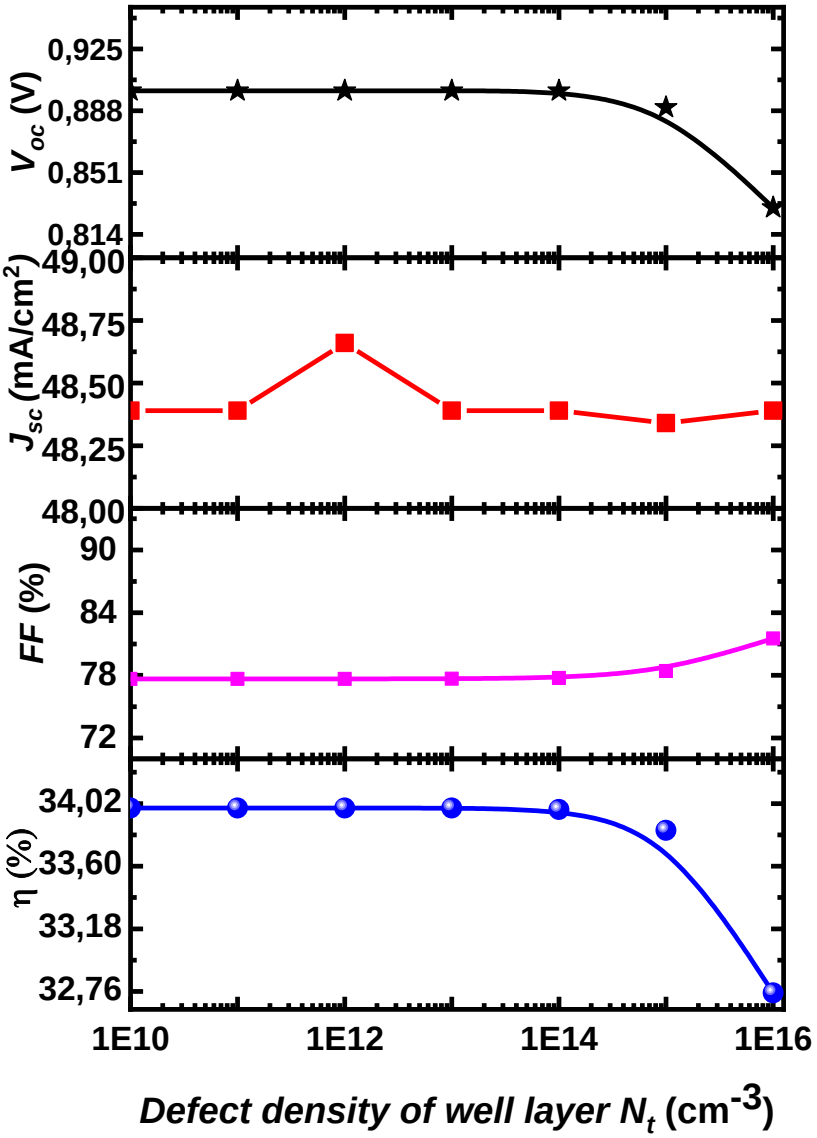

Figure III.14: Effect of defect density of well layer, N_t, on the CIGS QDSC performance.

The above results demonstrate that low levels of defect density do not significantly impair device performance. However, when the defect density exceeds a critical threshold, particularly beyond 10^{14} cm^{-3}, the photovoltaic parameters—especially *V*oc and η—deteriorate significantly. These findings emphasize the importance of minimizing defect density in the quantum well region to ensure high-efficiency solar cell operation.

III.8.6 Effect of CIGS Quantum Well Depth on Solar Cell Performance Parameters

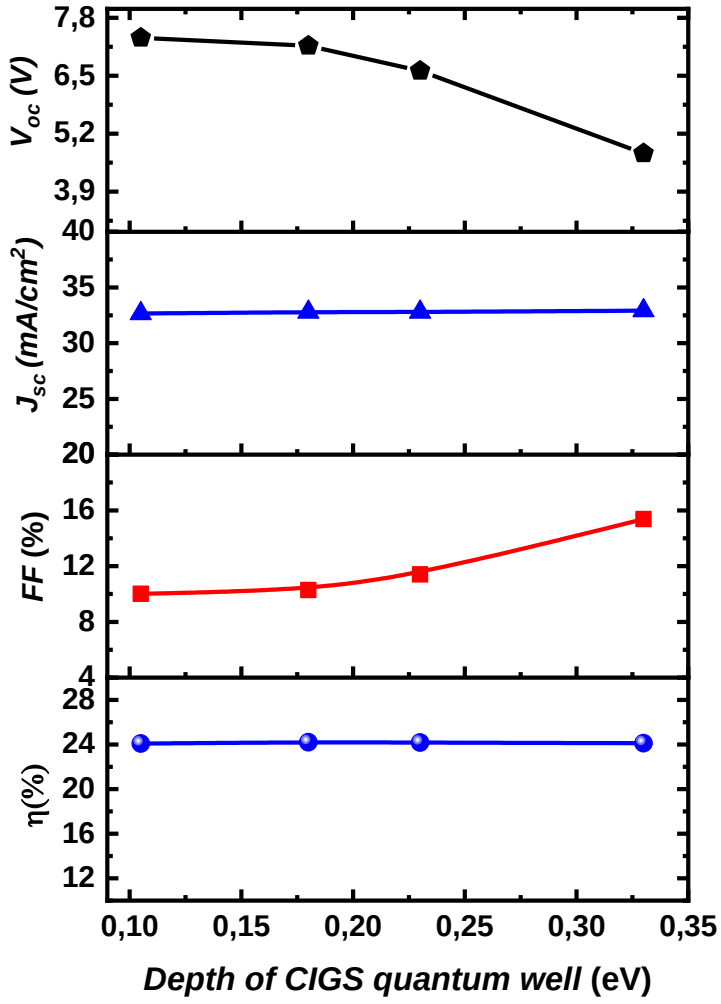

Figure III.15: Dependence of Solar Cell characteristics on the depth of CIGS quantum well.

The figure III.15 investigates the effect of the depth of the CIGS quantum well (in eV) on the main performance parameters of CIGS QDSC solar cell. As the depth of the CIGS well increases from 0.10 eV to 0.33 eV, the *V*oc decreases noticeably. This reduction may be attributed to increased carrier recombination or a weakened built-in electric field due to the deeper potential well. In contrast, the *J*sc remains nearly constant throughout the studied range. This stability suggests that the absorption of photons and carrier collection processes are not significantly influenced by changes in well depth.

Interestingly, the fill factor (*FF*) shows a slight increase with increasing well depth. This behavior could be explained by improved charge transport properties or a reduction in series

resistance as the potential well becomes deeper. Despite the decline in *V*oc, the conversion efficiency (η) remains stable, indicating a compensatory balance between the decreasing *V*oc and the increasing *FF*.

In conclusion, while a deeper CIGS well negatively impacts *V*oc, its effect on *J*sc and η is minimal, and it can even enhance *FF*. These results highlight the delicate trade-offs in optimizing quantum well structures for high-efficiency CIGS solar cells.

III.9 Conclusion

The study of quantum well solar cells based on $CuIn_{1-x}Ga_xSe_2$ (CIGS) absorbers demonstrates significant potential for enhancing photovoltaic performance. CIGS stands out as a versatile and efficient thin-film material due to its adjustable bandgap, strong light absorption, and stability under operating conditions. Incorporating quantum wells into the absorber layer can improve charge carrier separation and reduce recombination losses, leading to better efficiency.

The SCAPS-1D simulator proves to be an invaluable tool in this research, allowing researchers to model and optimize the complex physical processes within multilayer solar cell structures. By simulating different compositions, defect densities, and device architectures, SCAPS-1D helps predict performance outcomes without the immediate need for costly and time-consuming experiments.

Despite its advantages, SCAPS-1D has limitations, including its one-dimensional approach and reliance on accurate input parameters. Nonetheless, when used alongside experimental methods, it accelerates the development of innovative solar cells. Overall, combining advanced absorber materials like CIGS with quantum well engineering and powerful simulation tools such as SCAPS-1D represents a promising pathway toward achieving higher efficiency, lower cost, and more sustainable solar energy technologies in the near future.

References

[1] M. Burgelman, P. Nollet, S. Degrave,"Modelling polycrystalline semiconductor solar cells",*Thin Solid Films*, Vol. 361–362, pp. 527–532, 2000.

[2] S. Siebentritt, M. Ch. Lux-Steiner,"Non-stoichiometry and secondary phases in Cu(In,Ga)Se_2 absorbers",*Solar Energy Materials and Solar Cells*, Vol. 80, Issues 1–3, pp. 229–240, 2003.

[3] J. M. Kephart et al.,"Design and simulation of quantum well solar cells using CIGS materials",*IEEE Journal of Photovoltaics*, Vol. 5, No. 1, pp. 456–461, 2015.

[4] T. Minemoto, Y. Hamakawa,"Solar cell simulation using SCAPS-1D for different CIGS compositions",*Renewable Energy*, Vol. 28, pp. 819–826, 2003.

[5] A. Romeo, M. Terheggen, D. Abou-Ras et al.,"Development of thin-film Cu(In,Ga)Se_2 and CdTe solar cells",*Progress in Photovoltaics: Research and Applications*, Vol. 12, No. 2–3, pp. 93–111, 2004.

[6] H. W. Hillhouse, M. C. Beard,"Solar cells from colloidal nanocrystals: Fundamentals, materials, devices, and economics",*Current Opinion in Colloid & Interface Science*, Vol. 14, No. 4, pp. 245–259, 2009.

[7] SCAPS-1D User Manual, Ghent University – Department of Electronics and Solar Energy (ELIS), Access to the software and official documentation.

[8] H. W. Schock and J. H. Werner, "CIGS-based solar cells for the next century", *Solar Energy Materials and Solar Cells*, vol. 41-42, pp. 159–169, 1996.

[9] M. Gloeckler, J. R. Sites, "Band-gap grading in Cu(In,Ga)Se_2 solar cells," *Journal of Applied Physics*, vol. 98, 103703, 2005.

[10] S. Siebentritt, "Why are Cu(In,Ga)Se_2 solar cells so efficient?," *Solar Energy*, vol. 77, pp. 767–775, 2004.

[11] R. Scheer and H. W. Schock, Chalcogenide Photovoltaics: Physics, Technologies, and Thin Film Devices, *Wiley-VCH*, 2011.

General conclusion

General conclusion

Renewable energy plays a key role in the fight against climate change, as it comes from inexhaustible natural sources such as the sun, wind, or water, and helps reduce greenhouse gas emissions. It also promotes energy independence and job creation. Among these energy sources, photovoltaic (or solar) energy is particularly important: it converts sunlight into electricity using solar panels, without pollution or noise.

Photovoltaic cells, made of CuInGaSe2 (GIGS), are the basic components of these panels and make it possible to generate clean electricity from sunlight. This technology has become an economical, ecological, and sustainable solution.

The aim of our work is to optimize the CIGS solar cell performances using the quantum well technology. This study focused on the simulation and analysis of quantum well solar cells based on $CuIn_{1-x}Ga_xSe_2$ (CIGS) absorbers using the SCAPS-1D software. The introduction of quantum wells into the absorber layer aimed to enhance solar cell performance by extending light absorption into lower-energy regions and improving charge carrier collection.

Through the simulation process, we examined the influence of various parameters such as the number and thickness of quantum wells, the composition of the CIGS alloy, doping concentrations, and defect densities. The impact of these parameters on the photovoltaic behaviour of the cells was evaluated using standard metrics: short-circuit current density, open-circuit voltage, fill factor, and conversion efficiency. The results showed that quantum well structures can significantly improve the absorption capacity and photovoltaic performance of CIGS-based cells, provided that the physical and geometrical parameters are properly optimized.

The bandgap tuning through gallium content, as well as the careful control of well dimensions and defect levels, plays a key role in achieving high efficiency. This simulation work highlights the potential of quantum well architectures in next-generation thin-film solar technologies and opens perspectives for further research.

The integration of quantum wells (QWs) into CIGS solar cells has been demonstrated as a highly effective strategy for improving photovoltaic performance. The inclusion of QWs leads to significant enhancements in open-circuit voltage (Voc), short-circuit current density (Jsc), fill factor (FF), and overall power conversion efficiency (η), confirming their potential to push the efficiency limits of thin-film solar cells. However, the performance of quantum well solar

cells (QWSCs) is highly dependent on structural and material parameters, including well thickness, defect density, and well depth.

Increasing the well thickness improves light absorption and Jsc, but excessive thickness leads to higher recombination losses, reducing Voc. Thus, an optimal thickness must be identified to balance these competing effects. Similarly, defect density plays a critical role—while low defect concentrations have minimal impact, densities beyond 10^{13} cm^{-3} drastically degrade Voc and η, emphasizing the need for high-quality material growth. Additionally, deeper quantum wells reduce Voc but can improve FF, suggesting that well depth optimization can fine-tune device performance without sacrificing efficiency.

As a perspective:

- Further research should focus on defect passivation techniques to minimize non-radiative recombination in QWs.
- Exploring alternative quantum well materials or graded bandgap designs could enhance carrier extraction while maintaining high Voc.
- Future work may also include multidimensional simulations for more accurate modelling, as well as the fabrication and experimental validation of the proposed structures to assess their real-world viability.

Abstract:

This thesis presents a comprehensive numerical study of $Cu(In_{1-x}Ga_x)Se_2$ (CIGS)-based solar cells. It begins with a detailed examination of the structure, composition, and advantages of the CIGS material for photovoltaic applications. Using the SCAPS-1D simulator, several simulations are performed to assess the influence of key physical parameters—such as gallium content, absorber thickness, acceptor concentration, and defect density—on solar cell performance. The thesis also explores the integration of quantum well (QW) structures within the CIGS absorber. Numerical modeling of CIGS/QW devices evaluates the effect of quantum well thickness, defect levels, and well depth on the photovoltaic performance. The results provide valuable insights into optimizing CIGS-based solar cells, particularly through quantum engineering approaches.

Key words: Solar cell, Cu(In,Ga)Se2 absorber, Quantum well, Substrate structures, QWSC.

Résumé :

Ce mémoire présente une étude numérique approfondie des cellules solaires à base de $Cu(In_{1-x}Ga_x)Se_2$ (CIGS). Il commence par une présentation de la structure, de la composition et des avantages de ce matériau pour les applications photovoltaïques. À l'aide du simulateur SCAPS-1D, plusieurs simulations sont effectuées pour étudier l'effet de différents paramètres physiques, notamment la teneur en gallium, l'épaisseur de la couche absorbante, la concentration d'accepteurs et la densité de défauts, sur la performance des cellules. Le chapitre examine également l'intégration de structures de puits quantiques (QW) dans le CIGS. La modélisation numérique des dispositifs CIGS/QW analyse l'impact de l'épaisseur, de la concentration de défauts et de la profondeur des puits sur les performances photovoltaïques. Les résultats obtenus offrent des possibilités pour l'optimisation des cellules solaires CIGS, notamment par des approches de conception quantique.

Mot clés : Cellules solaires, Cu(In,Ga)Se2 absorber, Qauntum well, Structures substrates.

ملخص

يعرض هذا العمل دراسة عددية شاملة لخلايا شمسية تعتمد على مادة $Cu(In_{1-x}Ga_x)Se_2$ (CIGS). يبدأ بتوضيح بنية وتركيب هذا المركب ومميزاته في التطبيقات الكهروضوئية. باستخدام برنامجSCAPS-1D ، تم إجراء سلسلة من المحاكاة لدراسة تأثير عدة عوامل مثل نسبة الجاليوم، سمك طبقة الممتص، تركيز الشوائب المستقبلة، وكثافة العيوب على أداء الخلية الشمسية. كما يتناول الفصل دمج بنى الآبار الكمومية داخل طبقةCIGS ، ويتم تحليل التأثيرات المختلفة لسمك طبقة البئر، تركيز العيوب وعمق الآبار على كفاءة الخلية. تقدم هذه النتائج رؤى مهمة لتحسين أداء خلايا CIGS الشمسية، خاصة من خلال تقنيات الهندسة الكمومية.

الكلمات المفتاحية : الخلايا الشمسية، مادة $Cu(In,Ga)Se_2$ كممتص، البئر الكمومي، هياكل الركيزة.